2021

Distinguishing different styles of transpressional deformation at an obliquely convergent plate margin, Fiordland, New Zealand

Emily Sarah Lincoln
University of Vermont

Recommended Citation

Lincoln, Emily Sarah, "Distinguishing different styles of transpressional deformation at an obliquely convergent plate margin, Fiordland, New Zealand" (2021). *Graduate College Dissertations and Theses*. 1423.
https://scholarworks.uvm.edu/graddis/1423

DISTINGUISHING DIFFERENT STYLES OF TRANSPRESSIONAL DEFORMATION AT AN OBLIQUELY CONVERGENT PLATE MARGIN, FIORDLAND, NEW ZEALAND

A Thesis Presented

by

Emily Sarah Lincoln

to

The Faculty of the Graduate College

of

The University of Vermont

In Partial Fulfillment of the Requirements
for the Degree of Master of Science
Specializing in Geology

August, 2021

Defense Date: May 25, 2021
Thesis Examination Committee:

Keith A. Klepeis, Ph.D., Advisor
Kristen Underwood, Ph.D., Chairperson
Laura Webb, Ph.D.
Cynthia J. Forehand, Ph.D., Dean of the Graduate College

ABSTRACT

Fiordland, New Zealand provides one of the best-known and deepest (to 65 km) exposures of an Early Cretaceous magmatic arc root known to geologists. These exposures allow for us to study tectonic deformational processes at varying crustal depths, including the role of pre-existing structures on later reactivation. The well-preserved Grebe shear zone (GSZ) marks the boundary between major basement terranes in southern Fiordland and has undergone multiple episodes of deformation during the Cretaceous and Cenozoic time periods. The primary focus of this study is to recognize and characterize the differing phases of deformation that occurred along this shear zone. To investigate these phases, we have conducted structural, finite strain, fault-slip, and kinematic analysis, on structural measurements and samples taken from Fiordland. We use these methods in concert to identify and differentiate the deformational styles.

In southern Fiordland, the GSZ is characterized by a narrow zone of protomylonitic-mylonitic fabric within amphibolite retrogressed to greenschist facies rock. Finite strain analysis on feldspar aggregates from samples in and around the GSZ produced primarily oblate ellipsoids, indicative of shortening across the shear zone. Asymmetrical shear sense indicators present in thin sections oriented parallel, perpendicular, and oblique to lineations also suggest a component of sinistral obliquity in shear zone fabrics. This coupled with a deflection of foliations in surrounding rock towards parallelism with the shear zone boundary is consistent with transpressional deformation. This deformation is localized to a zone of ductile deformation where components of sinistral strike-slip and shortening are accommodated in close proximity to the shear zone (non-partitioned). This deformational event is associated with the formation of the shear zone and is overprinted by a separate transpressional event that took place during the Cenozoic. Fault-slip analysis showed that this reactivation event is accommodated in primarily brittle faults in where one set accommodates mostly or purely strike-slip motion, and another that accommodates mostly or purely reverse motion (partitioned). This contrasting style of transpression implies that the Cretaceous ductile shear zone influenced the behavior of strain during Cenozoic reactivation.

ACKNOWLEDGEMENTS

I have many people to thank for the completion of this thesis, the first being my advisor Keith Klepeis, for being a tremendous source of knowledge and support. Not only is he extremely knowledgeable and passionate about the subject, but he also genuinely cares about the success of his students. I could not have asked for a better mentor during my time in the program. I would also like to thank Laura Webb and for her support and help with the microstructure portion of my analysis, and Kristen Underwood for generously agreeing to be my chairperson in short notice. Within the UVM Geology Department, I would also like to thank John Hughes for his words of encouragement, which helped me immensely through both the program and the COVID-19 pandemic.

This project would not be possible without our collaborators, and I greatly thank Elena Miranda and Joshua Schwartz from CSUN, and Rose Turnbull and Richard Jongens from the New Zealand GNS for sharing their seemingly infinite knowledge both in the field and after. Lastly, I would like to thank my spouse, Stephen, for pushing me to pursue this in the first place, and for his help along the way.

TABLE OF CONTENTS

LIST OF TABLES

LIST OF FIGURES

CHAPTER 1: INTRODUCTION

Transpression is a style of deformation that is thought to be common in settings of oblique plate convergence (Hartland, 1971; Sanderson et al., 1984). Hartland (1971) originally defined transpression as a style that combines both compression and transcurrent faulting. The strain produced by these forces can either be localized (non-partitioned) or dispersed (partitioned) as several discrete structures (Dewey et al., 1998). Partitioned transpression accommodates movement by dispersing strain among different structures. For example, a transcurrent component can occur along strike-slip faults, with compression being accommodated by folding or thrust faulting. In contrast, a non-partitioned transpressional system localizes the strain in the area of shearing (Dewey et al., 1998). Differentiating between the styles of strain partitioning in transpressional systems holds importance in determining what processes deformed an area. Understanding deformation patterns associated with oblique convergence is integral in our understanding of plate tectonics as a whole because it is a common type of plate boundary (Teyssier et al., 1995). Geologists are unable to study present day oblique convergence in mid- and deep-crustal levels, therefore it is important that ancient, exhumed shear zones that record this type of deformation be fully characterized. Information gathered from past transpressional systems can be used to help predict future deformation patterns of active plate margins.

The structural controls imposed on strain partitioning have been widely discussed (Jones et al., 2005; Goodwin & Tikoff, 2002; Druguet et al., 2009; Fossen & Cavalcante, 2017). However, many different interpretations have been suggested for the controls in which deformation occurs along transpressional boundaries including temperature, pressure, and grain size (Goodwin & Tikoff, 2002). In addition, large contrasts in strength due to varying lithologies are typically found to be important in controlling how deformation is expressed (Goodwin & Tikoff, 2002). Upper-crustal shear zones are particularly interesting because they generally display wide heterogeneity with highly partitioned strain. As a result, one single ductile shear zone may be unable to accommodate the bulk strain of the entire deformational domain. Instead, several separate domains may be distributed spatially (Díaz-Azpiroz et al., 2014). This implies that the overprinting of brittle structures on already existing ductile fabrics can be the result of a change in transpressional style. The overarching goal of this study is to identify the type of transpression that occurred in our areas of interest, and to provide a better understanding of the controls imposed on the different styles of transpression.

Geologists rely on finding ancient examples of rocks exhumed from deep within the upper plate of a deeply convergent margin to study historical deformation patterns. Results of these studies aid in the interpretation of the behavior of active plate boundaries. A rare exposure of deep roots of the upper plate of an obliquely convergent margin in New Zealand allows for the direct observation of upper and lower crust interactions in an oblique convergent setting. Fiordland, New Zealand is part of the continent Zealandia, which is described as a partially submerged continental mass that was once part of the supercontinent Gondwana (Mortimer et al., 1999; Scott et al., 2011; Buriticá et al., 2019). Paleozoic to Mesozoic subduction-related magmatism created a long-lived magmatic arc on the edge of Gondwana. Later, extensional orogenic collapse in the Late Cretaceous resulted in rifting of Zealandia from Gondwana (Mortimer et al., 1999; Mortimer et al., 2017). A combination of Cretaceous extension and late Cenozoic reverse faulting resulted in the exhumation of the deepest known exposure of Early Cretaceous magmatic arc roots (Scott et al., 2011; Ducea et al., 2015; Klepeis et al., 2019). This rare exposure allows for the observation of differing styles of deformation at different crustal depths and has facilitated numerous studies on the mechanisms and styles of transpression (Scott et al., 2011; Schwartz et al., 2017; Buriticá et al., 2019). In present day, the Pacific Plate is actively thrusting over the Australian Plate along the prominent Alpine Fault, causing the rapid uplifting of the southern Alps (Figure 1) (Jiao et al., 2017).

Eastern Fiordland contains exposures of early transpressional shear zones, such as the Grebe shear zone (GSZ), one of several sinistral transpressional shear zones active during the Early Cretaceous (Scott et al., 2011, Buriticá et al., 2019). The GSZ is a 200 to 300 m-wide zone of mylonitic deformation with early low-strain fabrics (northern strand) and higher-strain mylonitic zones (southern strand). This shear zone represents the divide between the plutonic rocks of the late Cambrian to Cretaceous inboard and Early Carboniferous to late Mesozoic outboard belts of central and southern Fiordland (Scott et al., 2011; Buriticá et al., 2019). The GSZ is also superimposed by a series of brittle to semi-brittle faults that record a period of late Cenozoic transpression and reverse faulting (Scott et al., 2011). These structures will allow me to assess how earlier deformational events affect future events as an additional control on styles of transpression. Exposures of the shear zone at Lake Hauroko and Caroline Peak and of reactivation structures at Lake

Monowai, Borland Road, and Mount Watson allow for us to describe the behavior of this shear zone and structures associated with reactivation.

This project aims to characterize the transpressional nature of the GSZ and study the influence of ductile fabrics on reactivation caused by brittle faulting across shear zones. Key questions in this study include: (1) What style(s) of transpression characterize the Cenozoic and Cretaceous deformational structures? (2) What is the kinematic evolution of these deformational structures? and (3) What is the three-dimensional variability along and across strike in the formation of these structures? These questions were investigated by combining the results of structural, finite strain, kinematic, and fault-slip analysis. Previous studies on the GSZ have determined that the system exhibits a triclinic, non-partitioned transpressional style of deformation (Scott et al., 2011), however the southern portion has not been evaluated to the same extent. The results of our study suggest that the portion of the GSZ near Lake Hauroko and Caroline Peak underwent two phases of transpressional deformation. The first phase took place in the Cretaceous and records non-partitioned transpression of predominantly monoclinic symmetry, though some triclinic symmetry was observed. Reactivation of the shear zone occurred in the Cenozoic and records partitioned transpression in where shortening and strike-slip components are accommodated primarily across brittle faults.

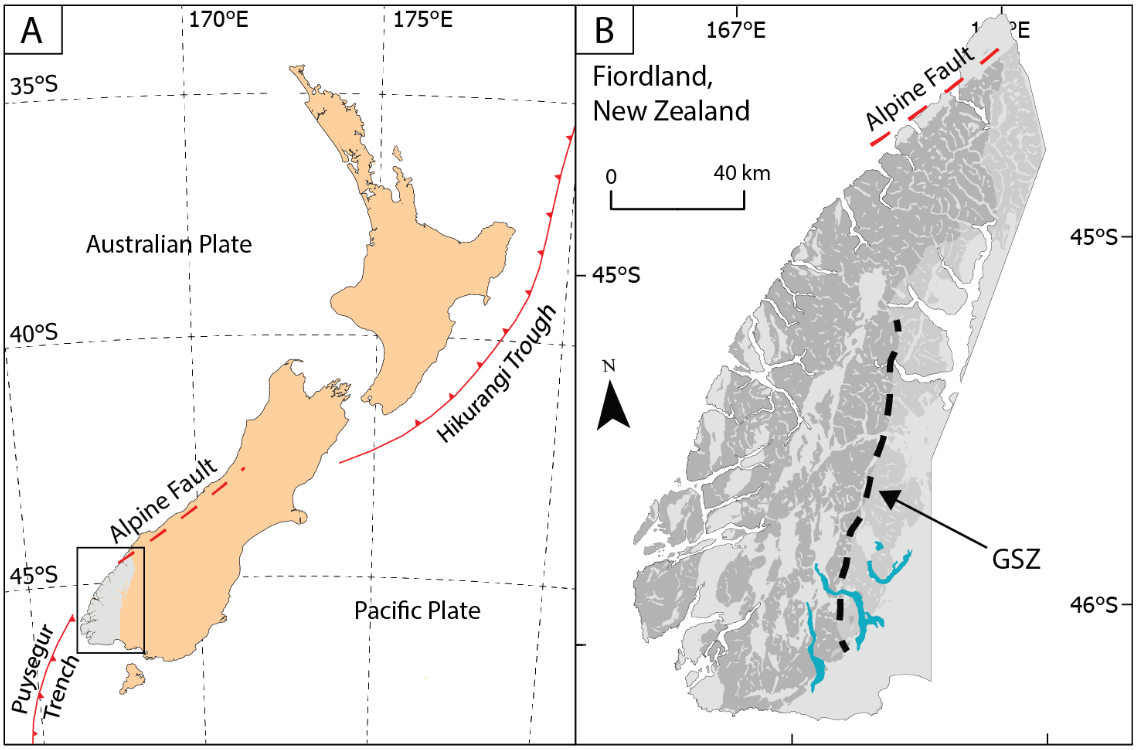

Figure 1. (A) Present day tectonic setting of New Zealand in where the Pacific plate is thrusting over the Australian plate near the Alpine Fault, and (B) map of Fiordland showing the Grebe shear zone (GSZ).

CHAPTER 2: LITERATURE REVIEW

2.1 Shear Zone Anatomy

In their most basic form, shear zones are represented by contrasting strain accumulation between the deformed zone and surrounding wall rock. At the surface, these structures present as fault zones, which accommodate movement within a narrow zone of discontinuous deformation (Vauchez et al., 2012). Deformation mechanisms within this zone are primarily brittle in nature (e.g., grain fracture, grain rotation) and strain is commonly localized. Beyond the brittle-ductile transition, the mechanisms of deformation progressively change to ductile (e.g., dislocation creep), and the zone is no longer characterized by discontinuous deformation, but instead by a zone of continuous deformation (Vauchez et al., 2012, Fossen and Cavalcante, 2017).

2.1.1. Transpressional/Transtensional Systems

Transpression and transtension are described as strike-slip deformations which involve a component of shortening or extension respectively, implying that both pure and simple shearing occur simultaneously during deformation (Dewey et al., 1998; Fossen et al., 1994; Sanderson & Marchini, 1984; Tikoff & Fossen, 1993). The combination of shearing produces finite strain, which creates distinct structures (foliations and lineations) that can be used to determine the nature of deformation (Fossen & Tikoff, 1994). Rocks containing pronounced foliations and lineations are known as LS-tectonites and are commonly found in transpressional and transtensional regimes (Fossen, 2010).

Finite strain can be described in terms of instantaneous stretching axes (ISAs) of the finite strain ellipse (FSE) produced during deformation. These axes represent the orientations and magnitudes of the maximum (X), intermediate (Y), and minimum (Z) stretching axes of the FSE and can provide valuable insight into strain behavior (Fossen et al., 1994). Sanderson and Marchini (1984) first quantified this type of deformation by using a matrix ($\boldsymbol{D}$) in where α^{-1} is shortening across the shear zone, α is the vertical stretch that results from this shortening, and γ is the shear strain parallel to shortening (Figure 2).

$$\boldsymbol{D} = \begin{pmatrix} 1 & \gamma & 0 \\ 0 & 1 & 0 \\ 0 & 0 & 1 \end{pmatrix} \begin{pmatrix} 1 & 0 & 0 \\ 0 & \alpha^{-1} & 0 \\ 0 & 0 & \alpha \end{pmatrix} = \begin{pmatrix} 1 & \alpha^{-1}\gamma & 0 \\ 0 & \alpha^{-1} & 0 \\ 0 & 0 & \alpha \end{pmatrix}$$

(simple shear) (pure shear) = (finite strain)

This matrix was further refined by Fossen and Tikoff (1993) to describe progressive deformation. Note that the variable defined initially as shortening across the shear zone (α^{-1}) is modified to instead represent the shape of the ellipsoid using the Flinn k-value.

$$\boldsymbol{D} = \begin{pmatrix} 1 & \dfrac{\gamma(1-k)}{\ln{(k^{-1})}} & 0 \\ 0 & k & 0 \\ 0 & 0 & k^{-1} \end{pmatrix}$$

Using this matrix, a relationship between shortening/extension (k) and the shape of the FSE can be discerned in where $k < 1$ produces oblate strains, $k = 1$ produces plane strains, and $k > 1$ produces prolate strains (Tikoff & Fossen, 1993; Sanderson & Marchini, 1984). This relationship can be plotted on a Flinn diagram in where the relative ratios of the FSE axes are plotted on each axis, however it presents its own limitations, such as clustering of low strain data points. Instead, we use a polar Nadai-Hsu plot, which is advantageous because it incorporates natural (logarithmic) strain (ε) into the calculation of the FSE (Hossack, 1968).

Introducing simple shear to a system subsequently induces a component of rotation, which can be quantified using the kinematic vorticity number (W_k). This value is directly related to the orientation of the FSE because it quantifies the coaxiality of progressive deformation in where $W_k = 1$ represents simple shearing (rotational), and $W_k = 0$ represents pure shearing (non-rotational) (Means et al., 1980; Tikoff & Fossen, 1993). This can be used to determine if a transpressional or transtensional system is dominated by pure or simple shear and is associated with specific fabric and strain characteristics (Table 1). In the case of transpression, oblate strains produce S- and LS-tectonites, however the orientation of these structures depends on W_k. For example, in pure shear dominated transpressional systems, the orientations of stretching lineations are close to vertical, whereas in simple shear dominated systems, their orientations are closer to horizontal. Because strain is flattening, the orientations of foliations with respect to the shear zone boundaries does not change with W_k. The opposite is true of transtensional systems that produce primarily L- and LS-tectonites. Lineation orientations remain horizontal or oblique to the shear zone boundary while foliation orientations vary from nearly vertical to horizontal with increasing W_k (Fossen et al., 1994).

Rotation of the axes of the FSE can produce sense of shear indicators that can be used to determine deformational symmetry. Symmetry can be divided into two broad categories, triclinic and monoclinic, which are distinguished by the behavior of strain during deformation. Monoclinic (two-dimensional) symmetry is the result of the rotation of two principal axes of finite strain, whereas triclinic (three-dimensional) is the result of all three axes of finite strain rotating about a fixed point (Dewey et al., 1998). Deformational symmetry can therefore be determined by using finite strain and kinematic analysis in concert with one another. The use of both methods is crucial because no one method can determine the symmetry, and the behavior of finite strain greatly influences the behavior of shear sense indicators (Díaz-Azpiroz et al., 2019). For example, if strains exhibit monoclinic symmetry, asymmetric shear-sense indicators will only be visible on one surface of a sample. This is also known as two-dimensional symmetry because it assumes that deformation is dominated by simple shear and that shear zone boundaries are vertical (Díaz-Azpiroz et al., 2019). In contrast, triclinic symmetries can produce asymmetric shear sense indicators on multiple surfaces. This is also known as three-dimensional symmetry, or inclined transpression, because it involves a larger component of pure shear and the shear zone boundaries vary from vertical (Figure 4) (Díaz-Azpiroz et al., 2019; Jones et al., 2004).

Strain can also be dispersed among different structures (partitioned) or localized into one zone of deformation (non-partitioned) within transpressional/transtensional systems (Figure 5). The structural controls imposed on strain partitioning have been widely discussed (Jones et al., 2005; Goodwin & Tikoff, 2002; Druguet et al., 2009; Fossen & Cavalcante, 2017). In particular, Jones and Tanner (1995) describe structural and mechanical anisotropies as being important controls on strain partitioning. These anisotropies are typically weaknesses in the rock created by faults, shear zones, or lithologic boundaries where strain can be preferentially accommodated.

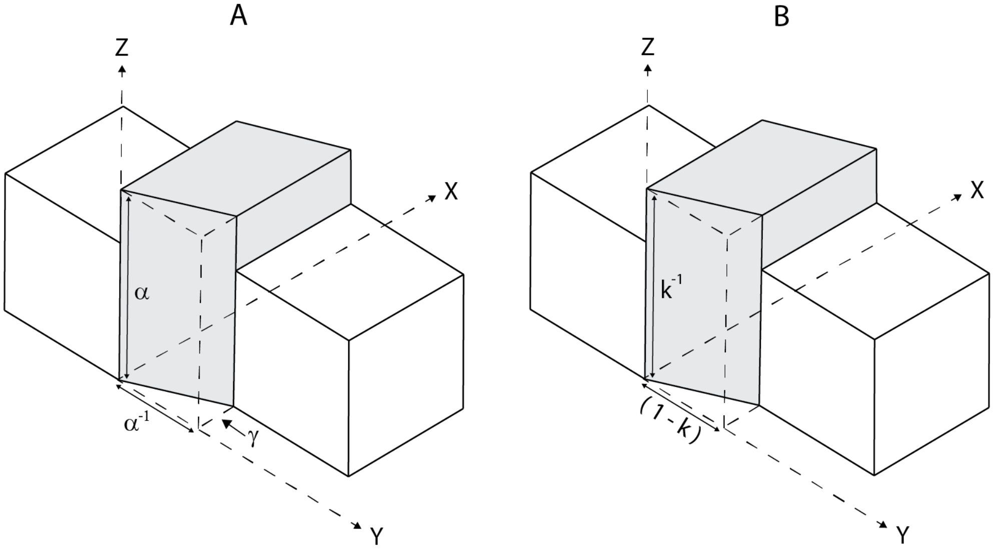

Figure 2. Variables associated with the deformation matrix described by Sanderson and Marchini (1984) (A) and Fossen and Tikoff (1993) (B). Adapted from Fossen and Tikoff (1993) (B). Adapted from Fossen and Tikoff (1993).

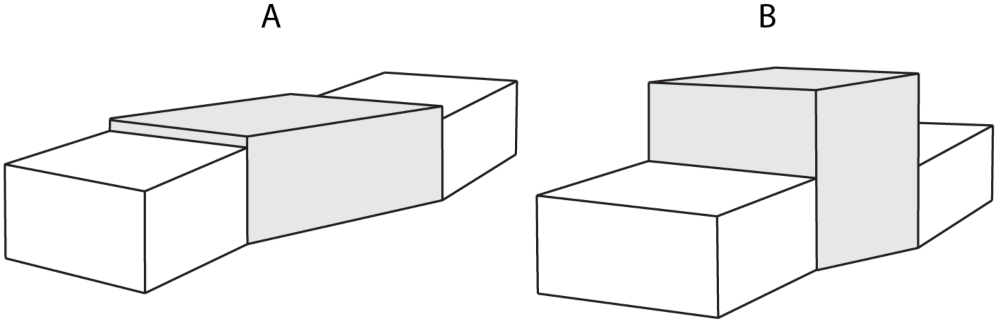

Figure 3. Simple-shear (A) vs. pure-shear (B) dominated transpression. Adapted from Fossen et al. (1994).

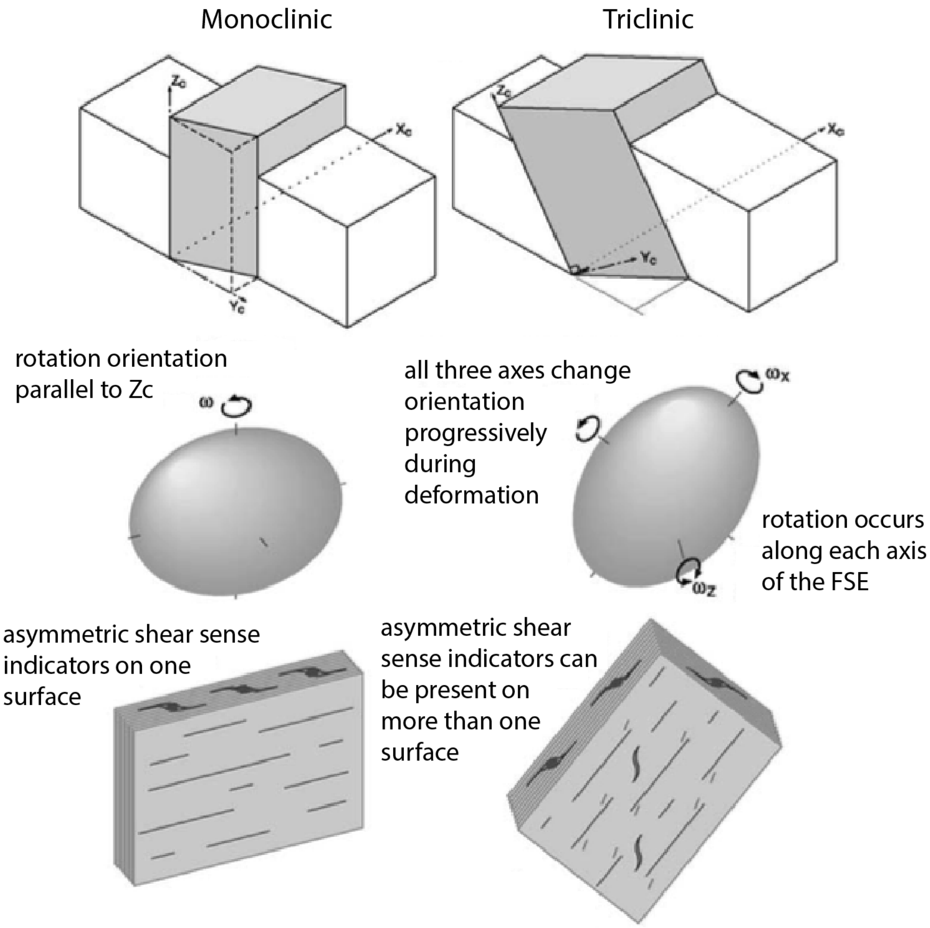

rotation orientation parallel to Zc

all three axes change orientation progressively during deformation

rotation occurs along each axis of the FSE

asymmetric shear sense indicators on one surface

asymmetric shear sense indicators can be present on more than one surface

Figure 4. Monoclinic (2D) vs. triclinic (3D) symmetry with respect to the FSE and sense of shear indicators. Adapted from Jones et al. (2004).

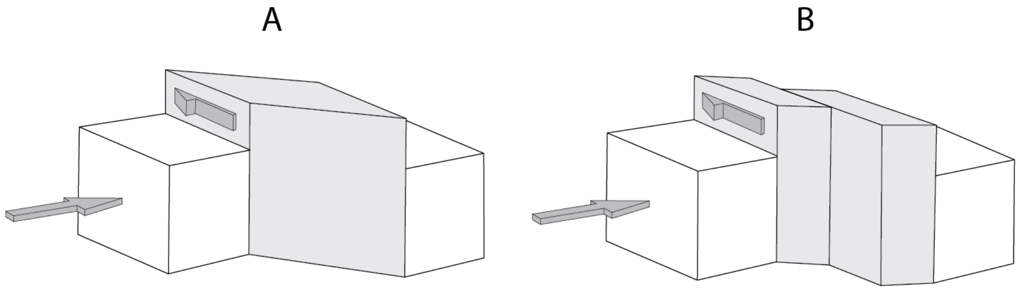

Figure 5. Non-partitioned (A) strain where simple and pure shearing are accommodated along the same structure, and partitioned (B) strain, where simple and pure shearing are accommodated along discrete structures. Adapted from Teyssier et al. (1995).

Transpression

	Pure Shear (Contraction)	Pure Shear Dominated		Simple Shear Dominated	Simple Shear
	$W_k = 0$		→		$W_k = 1$
Fabric	LS	(L)S	S	(L)S	LS
Stretching Lineation	vertical	vertical	none – weak vertical	horizontal – oblique	horizontal – oblique
Foliation	vertical – parallel	vertical – oblique	vertical – oblique	vertical – oblique	vertical – oblique
Strain	plane	oblate	oblate	oblate	plane

Transtension

	Pure Shear (Extension)	Pure Shear Dominated		Simple Shear Dominated	Simple Shear
	$W_k=0$		→		$W_k = 1$
Fabric	LS	L(S)	L	L(S)	LS
Stretching Lineation	horizontal – perpendicular	horizontal – oblique	horizontal – oblique	horizontal – oblique	horizontal – oblique
Foliation	horizontal	vertical – oblique	none – weak horizontal	horizontal	vertical – oblique
Strain	prolate	prolate	prolate	prolate	plane

Table 1. Table adapted from Fossen et al. (1994) generalizing the relationship between W_k and physical characteristics.

2.2. Geologic Background of Fiordland

Zealandia was first recognized by Luyendyk (1995) as a partially submerged continental mass that previously joined the Gondwana supercontinent. Paleozoic to Mesozoic subduction-related magmatism created a long-lived magmatic arc on the edge of Gondwana. Later, extensional orogenic collapse in the Late Cretaceous resulted in rifting of Zealandia from Gondwana (Mortimer et al., 1999; Mortimer et al., 2017). A combination of Cretaceous extension and late Cenozoic reverse faulting resulted in the exhumation of the deepest-known exposure of Early Cretaceous magmatic arc roots in Fiordland, New Zealand (Scott et al., 2011; Ducea et al., 2015; Klepeis et al., 2019). In present day, the Pacific Plate is obliquely thrusting over the Australian Plate along the prominent Alpine Fault, subsequently causing the rapid uplift of the Southern Alps (Figure 1) (Jiao et al., 2017). This area is of particular interest because it allows geologists to directly study transpression, which is a common style of deformation at obliquely convergent margins.

Episodic subduction and subsequent magma pulses at the Gondwana margin in the Mesozoic created the largest contiguous area of plutonic rock in New Zealand. This area is known as the Median Batholith, which is described as a composite batholith that encompasses several smaller Devonian to Early-Cretaceous plutons (Mortimer et al., 2017). Though the term batholith is used for the entire 10,200 km^2 area of plutonic rock, it is important to note that within it are a wide variety of lithologies, ages, and metamorphic regimes (Mortimer et al., 1999). The rocks comprising the Median Batholith are subdivided into two belts of rock, the eastern inboard and western outboard belts, by the Grebe shear zone (GSZ) to the south and the Indecision Creek Shear Zone (ICSZ) to the north (Mortimer et al., 1999; Buriticá et al., 2019) (Figure 6). The Median Batholith also represents the divide between the early Paleozoic to Mesozoic accreted basement terranes of Fiordland. Our area of interest is the southern portion of the GSZ, where the batholith separates the metasedimentary and volcaniclastic Brook Street Terrane and the largely paragneissic western Takaka Terrane, which coincide with the inboard and outboard belts respectively (Mortimer et al., 1999; Mortimer, 2004; Scott et al., 2011; Scott, 2013). Late Cenozoic reactivation of the shear zone caused the overprinting of brittle to semi-brittle structures throughout portions of the GSZ (Scott et al., 2011), which allows for us to study the effect of pre-existing boundaries on reactivation.

The portion of the GSZ near Lake Manapouri has previously been described as an amphibolite facies shear zone that accommodated sinistral reverse-slip motion (Scott et al., 2011) and sinistral motion (Buriticá et al., 2019). In addition, Buriticá et. al (2019) concluded that the western boundary of the shear zone near Lake Manapouri exhibits an apparent normal (west-side-down) sense of motion and predicted a thrust-sense motion on the eastern boundary, which is predicted by inclined transpression. Marcotte et al. (2005) determined that the boundaries of the northern IDCZ exhibit sinistral oblique-slip and dip-slip displacements in the lower crust. However, orientations of fabrics were observed to change in concert with increasing strain, with rotating and steepening foliation surfaces and increasing pitch of associated mineral lineations.

The GSZ provides an ideal location to study not only the behavior of shear zones at depth, but also the influence of pre-existing weaknesses on strain partitioning. The GSZ represents the boundary between two basement terranes, is the divide between the inboard and outboard Median batholiths, and has undergone deformational changes in response to changing regional stress. The exposure of the shear zone and its complex deformational history allow for in-depth characterization of the deformational effects of oblique convergence and reactivation.

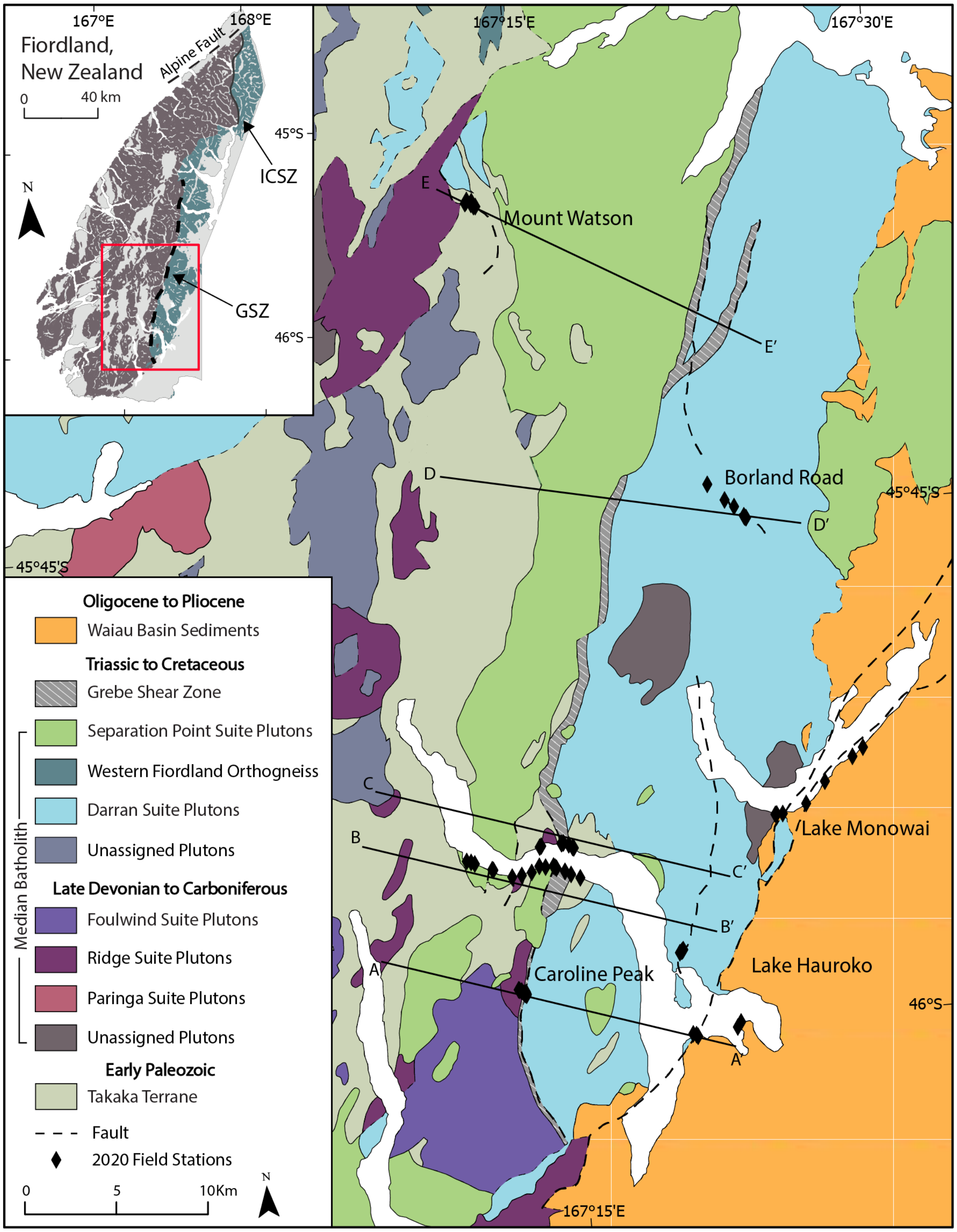

Figure 6. Figure of study area in southern Fiordland, New Zealand. Formation information including age, location, and suite from Turnbull et al., 2010. Cross-sections associated with A-A’, B-B’, and C-C’ can be found in Figure 9. Cross-sections associated with D-D’ and E-E’ can be found in Appendix A.

CHAPTER 3: METHODS

3.1 Field Work & Data Collection

Field work in southern Fiordland was conducted in January of 2020 with the primary goal of transecting the GSZ. Secondary to this, we were in search of evidence of multiple episodes of deformation related to later Cenozoic overprint of brittle structures. Localities exhibiting ductile shearing include Mount Watson, Lake Monowai, Caroline Peak, Borland Road, and Lake Hauroko (Figure 6). Brittle structures were also observed at Lake Monowai, Caroline Peak, Mount Watson, and Borland Road. Measurements of foliations, lineations, bedding, fault planes, fold axes/axial planes, and/or fold limbs were taken using a Brunton Compass and plotted using Allmendinger's Stereonet Mobile app at 58 stations. In addition to structural measurements, 61 rock samples were collected and cut prior to their transport to campus for structural, strain, and/or microstructural analysis depending on the structures observed (brittle vs. ductile).

3.2 Structural & Microstructural Analysis

3.2.1 Fabric and Reactivation Characterization

In the context of this thesis, the term “fabric” is used primarily to describe structures and textures formed via ductile deformation, including foliations, lineations, intrafolial folds and the mineral assemblages and textures that define them. Fabrics were characterized both in hand sample and in thin section with the primary goals of assessing their 3-D orientation, kinematic evolution, and the finite strain state.

Similar to that of Klepeis et al. (2019), we use the term “reactivation” to describe a change in movement kinematics associated with overprinted structures. The purpose of establishing this definition was to differentiate kinematic changes over geologic time from those that occurred simultaneously within the same zone of deformation. Evidence for reactivation was characterized at the outcrop and thin section scale and most commonly included fracturing deforming foliation.

3.2.2 Structural Analysis

Structural analysis involved using data collected in the field to create cross-sections, stereographic projections, and maps to reconstruct the 3-D structure of each transect and the kinematic evolution of deformation features. Measurements of foliation and lineation are most relevant when characterizing finite strain across the GSZ. To visualize these data, foliations and lineations were plotted on equal area, lower-hemisphere stereographic projections using *Stereonet 11.0* (Allmendinger et al., 2012; Cardozo & Allmendinger, 2013). Specifically, measurements from Lake Hauroko and

Caroline Peak where the GSZ was encountered were projected according to site locality. Representative foliation measurements for each locality were determined by first using the Kamb contouring method of the poles to the foliation planes to identify outliers in the data. This method directly incorporates statistical analysis in that the contours are represented as standard deviations from a uniform distribution of all of the points being contoured (Kamb, 1959) and is therefore useful in determining representative populations of measurements. The representative measurement for each station was then found by calculating the mean vector of the conforming population and choosing the data point that most closely matched this orientation (Fisher et al., 1993).

Using these measurements together with field observations of cross-cutting relationships and other structural measurements, cross-sections transecting the GSZ were created across Caroline Peak and the north and south shores of Lake Hauroko. Two additional cross sections were constructed transecting Borland Road and Mount Watson using the same process for identifying representative measurements. These cross-sections were used primarily to evaluate the three-dimensional structure of each transect, with less emphasis on assessing a strain gradient, and can be found in Appendix A (pg. 82). Additional information on bedrock and surface geology was obtained from the 1:250000 geological map of Fiordland (Turnbull et al., 2010) and used to aid in the creation of cross-sections and regional maps.

3.2.3 Microstructural Analysis

Microstructural analysis was used to further characterize fabrics, their kinematics, and to determine the sequence of multiple fabrics in a sample, which cannot always be determined at outcrop and hand sample scale. Thin sections were prepared perpendicular to foliation and lineation and/or perpendicular to foliation and parallel to lineation in order to ensure that faces of maximum and minimum strain could be observed, and a petrographic macroscope was used to view the sections at varying magnifications. Mineral assemblages and mineralogy associated with fabric development were recorded. Due to the abundance of quartz and felspar in the samples, indicators of deformation such as undulose and checkerboard extinction, bulging recrystallization, and grain boundary migration were more readily observed in these minerals.

3.2.4 Shear Sense Determination

Determining sense of shear aids in the interpretation of structural symmetry where shear zone fabrics displaying monoclinic symmetry show asymmetric structures on surfaces that parallel the XZ plane. Shear zones displaying triclinic symmetry show asymmetric structures on multiple surfaces within the X, Y, Z reference frame (Dewey et al., 1998). Sense of shear was determined by observing offset markers and asymmetrical structures in both hand sample and in thin section. Asymmetrical structures include mica and hornblende fish, plagioclase feldspar porphyroclasts with asymmetric strain shadows composed of primarily quartz and biotite, lattice preferred orientation in quartz, and quartz-biotite shear bands.

3.3 Finite Strain Analysis

Finite strain analysis was conducted on several samples exhibiting ductile deformation from Lake Hauroko and Caroline Peak in order to assess the two-dimensional strain ellipse and, if possible, three-dimensional strain ellipsoid of the fabric. For the purposes of this thesis, we have conducted finite strain analysis with the goal of comparing strain across the shear zone. Analysis was performed on carefully selected samples using the program *EllipseFit 3.8.0* (Vollmer, 2018), in where a best fit ellipse is assigned to each analyzed face of a sample by the well-established R_f/ϕ method (Lisle, 1985), and a strain ellipsoid is calculated using these section ellipses. Section ellipses and subsequent ellipsoids are fit by manually outlining aggregates of strained minerals, in our case primarily feldspars, which represent passive strain markers. Figure 7 provides an example of the steps and results of evaluating the shape and orientation of the finite strain ellipsoid.

3.3.1 Sample Selection

Samples having undergone finite strain analysis were selected based several parameters including their degree of fabric development, grain size, location, etc. Grain size was of particular importance in the selection process, as individual aggregates are manually outlined in the program. As a result, samples with well-developed fabrics (ex. fine-grained mylonite) were not necessarily viable options for this particular analysis. The distribution of samples used in this analysis is therefore focused on areas around Lake Hauroko and Caroline Peak where we encountered the GSZ. In order to assess the strain gradient across the GSZ, strain analysis was performed on samples both in and out of the shear zone. Samples were trimmed at the GNS in Dunedin, New Zealand at angles approximately perpendicular to foliation and parallel to lineation, and parallel to both foliation and lineation. The purpose of trimming the samples in this manner was to ensure that the faces exhibiting the both the highest (XY) and lowest (YZ) degree of stretching could be viewed. Hand samples were re-oriented according to field measurements and the orientation of each face being analyzed was taken. High resolution scans of each face were taken using a flatbed scanner and rotated to ensure that the strike of the plane was horizontal and pointed to the right. Thin section samples were photographed at 5.8x magnification using an AmScope MU1000 digital microscope camera attached to a Leica M420 macroscope. These images can then be loaded directly into *EllipseFit*, where the user can then choose individual grains to be used as passive strain markers.

3.3.2 2D Strain Ellipses: The R_f/ϕ Method

Individual grains of feldspar (hand-samples) and quartz (thin-sections) were outlined using the shape function in *EllipseFit*, which were then mathematically converted to moment-equivalent ellipses (Vollmer, 2018). The program simultaneously populates a data table with the local coordinates, maximum and minimum radii, and area of each ellipse. The calculated ellipses are then plotted on the R_f/ϕ plot, where R_f represents the ratio of the maximum to minimum radius of the selected ellipse, and ϕ represents the final orientation of the ellipse with the long axis being oriented clockwise from the X-axis. The latter two parameters are calculated by *EllipseFit* and subsequently used when calculating the best fit section ellipse.

The two-dimensional best fit section ellipse is calculated using a series of linear equations which produce a resultant shape matrix containing eigenvectors and eigenvalues. Eigenvectors represent the orientations of the ellipse axes (X, Y, and Z), and eigenvalues represent the magnitude of these axes (Shimamoto & Ikeda, 1976). The calculation and comparison of these matrices provides insight into the shape and orientation of the section ellipse. For example, equal eigenvalues of the X and Y would produce an oblate ellipse, whereas equal eigenvalues of the Y and Z would produce a prolate ellipse (Díaz-Azpiroz et al., 2014). The distinction between prolate and oblate ellipses is important when defining deformation style, as transpressional deformation involves flattening strain and would therefore be represented by oblate ellipses (Sanderson & Marchini, 1984). Similarly, transpressional symmetry can be determined by the eigenvectors of the ellipses, where a rotation of one axis of finite strain would represent monoclinic symmetry, and a rotation of all three axes of the finite strain ellipsoid would represent triclinic symmetry (Dewey et al., 1998).

3.3.3 3D Strain Ellipsoids: Robin & Shan Methods

The aforementioned method is robust for calculating a two-dimensional strain ellipse but does not take volumetric strain into account. Two methods for calculating the three-dimensional strain ellipsoid are embedded within *EllipseFit* as described by Robin (2002) and Shan (2008). Both methods require a minimum of three section ellipses in order to perform a best fit ellipsoid calculation. Ideally these faces would represent the maximum and minimum stretching directions (X and Z), however it has been found that robust ellipsoids can also be generated by using faces cut at high angles to one another

(Vollmer, 2018). Both methods implement a system of linear equations to calculate the trend and plunge and degree of stretching of ellipsoid axes, however Shan's method allows for the use of stretching lineation data by the implementation of additional linear equations for each section ellipse or lineation measurement (Shan, 2008). These methods were compared by Vollmer (Vollmer, 2010), who concluded that the differences in the calculated strain ellipsoids are negligible. During our analysis, we found that the degree of error was smaller on hand samples using the Robin method. However, in thin section the Shan method produced smaller confidence intervals. Therefore, we implemented the Robin method for all hand samples analyzed, and the Shan method for all thin section samples analyzed.

Calculated strain ellipsoids are displayed on Nadai-Hsu plots, which provides a visual representation of the magnitude (ε_o) and symmetry (v) of imposed strain. This particular plot is useful in visualizing the ellipsoid because the symmetry is represented by Lode's ratio (v) in where -1 represents a prolate ellipsoid, and 1 represents an oblate ellipsoid. The plot also has the ability to display confidence regions, making it useful for comparing strain data from multiple samples. Alternatively, the ellipsoids can be visualized using shade plots, which mimic the shape and orientation of the ellipsoid (Figure 7).

3.3.4 Error Analysis

Bootstrap resampling was automatically performed on all section ellipses and sample ellipsoids to produce confidence regions. This technique involves random resampling with replacement of the data (in our case, 5,000 times) to create 95%

confidence intervals on ellipsoid axes and orientations. Another useful form of error analysis was performed by comparing the orientations of the ellipsoid axes with field measurements. When plotted on an equal-area lower hemisphere stereonet, the direction of maximum stretching (X) should align with plotted lineations, and the minimum stretching direction (Z) should plot close to the poles of foliations.

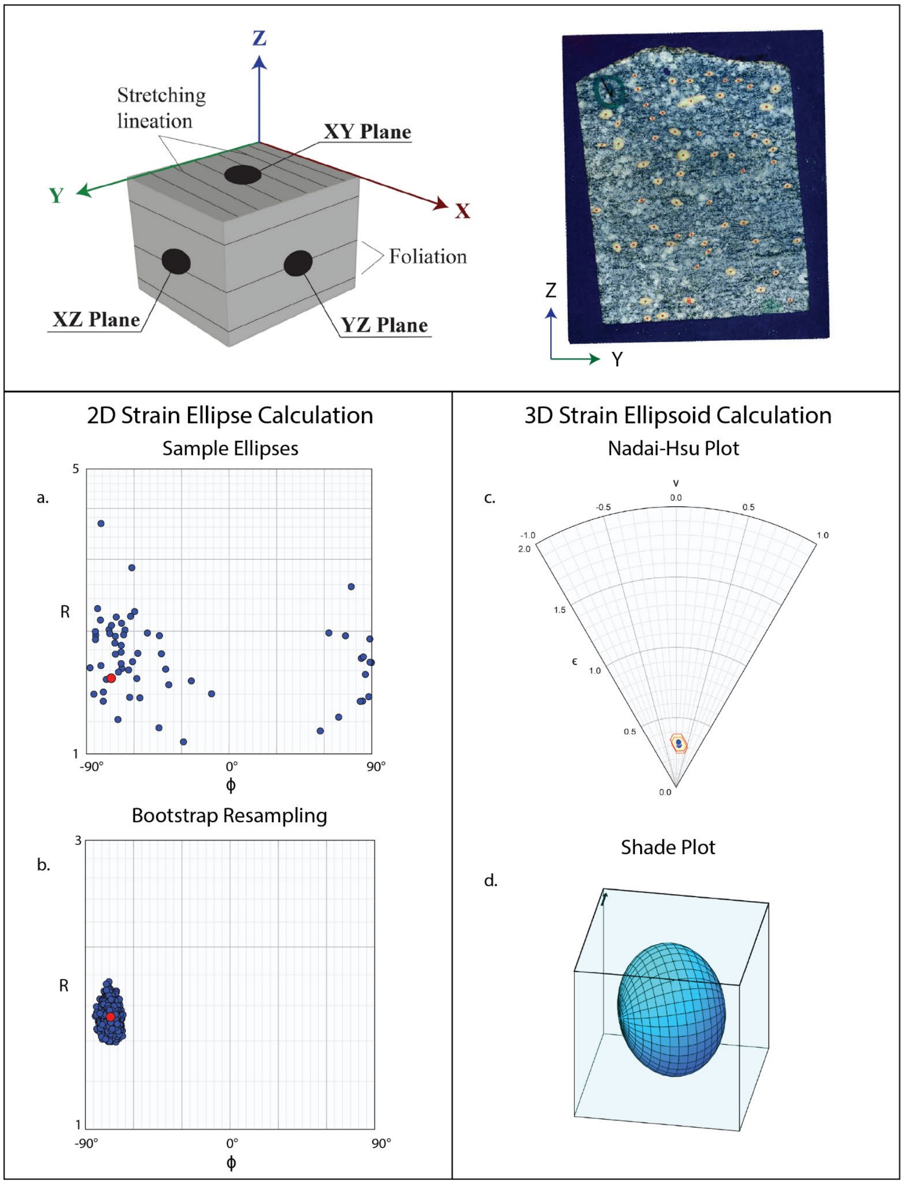

Figure 7. An example of the procedure for quantifying finite strain. Sample faces are cut approximately orthogonally to each other, ideally exposing the faces of maximum (XZ) and minimum (YZ) stretching. Aggregates are outlined in *EllipseFit* for each face, producing an R_f / ϕ plot (a) with each data point in blue and the mean in red. Plot b is the result of bootstrap resampling. This process is repeated for all faces of the sample, and the resulting average R_f and ϕ values are used in three-dimensional strain analysis. The Nadai-Hsu plot (c) shows the results of the best fit ellipsoid calculation in red with the 95% confidence interval highlighted in yellow. This particular plot shows two very similar ellipsoids that are the result of performing both the Robin and Shan methods using the same section ellipses. The final plot (d) is a shade plot generated by *EllipseFit* displaying the section ellipse three-dimensionally.

3.4 Fault-Slip Analysis

Analysis on overprinted brittle structures was performed by quantifying instantaneous strain using the program *FaultKin 8.1,* which allows the user to input fault related data to calculate the principal shortening and extension axes of fault populations (Allmendinger et al., 2012; Marrett & Allmendinger, 1990). The axes of shortening and extension can then be displayed graphically as a fault plane solution, which allows for an intuitive way of visualizing fault movement. This method provides an alternative way of displaying fault-slip data and is not interpretive. Block diagrams of major faults from each field locality were constructed using *Blender 2.9.2* to further illustrate fault behavior.

3.4.1 Fault Classifications

Fault populations were delineated by using field notes of cross-cutting relationships and equal area lower-hemisphere stereographic projections of plane and slickenline orientations. Kinematic characterization of faults requires complete fault-slip datum, which includes the orientation of the fault plane, the direction of slip, and the sense of slip (Marrett & Allmendinger, 1990). Due to the nature of field work, it was not possible to obtain complete fault-slip data for all faults observed. Therefore, incomplete fault-slip data were not included in the calculation of kinematic tensors. However, these faults were included when discerning fault populations when appropriate. The major population for each field area was determined based on the abundance of measurements taken and field notes of dominant fault sets. Fault kinematic analysis was performed on the dominant population from each area. Comprehensive fault data and subordinate populations can be found in Appendix C (pg. 95), where the three largest population for each field locality are identified.

3.4.2 Fault Plane Solutions

Fault kinematics were analyzed graphically using fault plane solutions generated in *FaultKin*. The program allows for kinematic tensors to be calculated using the linked Bingham or Moment Tensor methods as described by Allmendinger et al. (2012) and Marrett and Allmendinger (1990). For the purposes of this thesis, we chose the former, as the moment tensor method is commonly used in seismic studies. Average fault plane solutions were constructed for each population of faults and display the average fault plane and the shortening (P-) and extension (T-) axes on an equal area lower-hemisphere stereonet. These axes are plotted on the same plane as the slip direction and pole to fault, known as the movement plane, creating 45° angles with each (Marrett and Allmendinger, 1990) (Figure 8). Distinguishing the sense of slip is important in this approach to differentiate between each of these axes. This method assumes that the magnitudes of deformation are uniform across all faults being analyzed, which is why grouping faults into distinct populations is imperative prior to this analysis.

Using this method aids in our determination of kinematic tensors of fault data given that the extension axis is X, and the shortening axis is Z. The intermediate axis (Y) is represented by the intersection of the measured fault plane with its' theoretical complementary shear plane, which is oriented orthogonally to the fault plane (Fossen, 2010). It is important to acknowledge that the kinematic tensors are not necessarily equal to the directions of maximum (σ_1) and minimum (σ_3) stress. However, σ_1 and σ_3 must lie within the P- and T- fields respectively, meaning that stress directions can be reasonably estimated given a robust data set (Fossen, 2010).

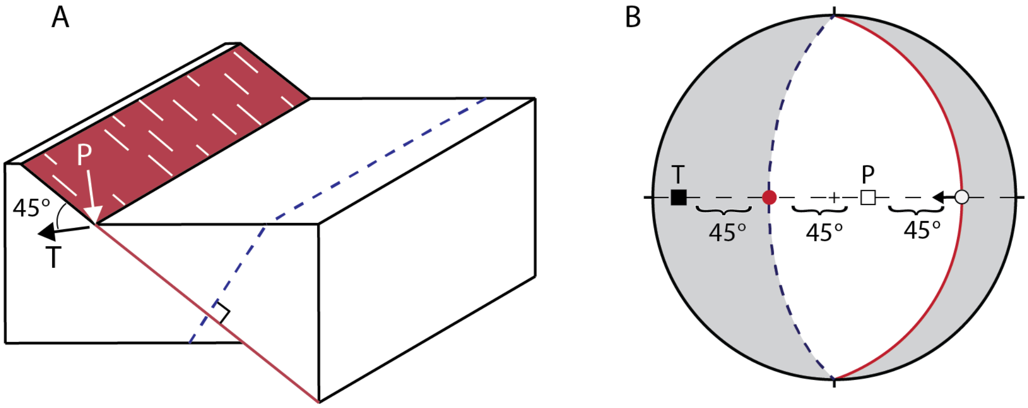

Figure 8. Block diagram (A) and associated fault plane solution (B) with P- and T- fields. The red plane (B) represents the slip surface, slickenline (hollow line), and movement vector (arrow). Horizontal dashed line represents the movement plane. Adapted from Fossen (2010).

CHAPTER 4: RESULTS

4.1 Anatomy of the Grebe Shear Zone

There are three locations where we encountered the Grebe Shear Zone (GSZ). From north to south they are Lake Hauroko North Shore, Lake Hauroko South Shore, and Caroline Peak. Three transects were completed across the shear zone at these locations (Figure 9). Measurements of planar features including foliations, bedding contacts, and faults, taken during this field season as well as from prior studies (Turnbull et al., 2010) were used to construct cross sections across these transects (Figure 10). These cross sections allow us to infer and interpret the subsurface structure of the GSZ along the strike of the shear zone boundary, and to observe spatial changes that occur throughout. The two most notable spatial differences are changes in apparent thickness of the shear zone from Caroline Peak to Lake Hauroko and changes in the dip of the shear zone. Additionally, the GSZ is reactivated by a zone of brittle faulting at both locations, however the bounding side changes from the eastern at Caroline Peak to the western at Lake Hauroko. This is accompanied by a change in dip direction from east at Caroline Peak, to west at Lake Hauroko.

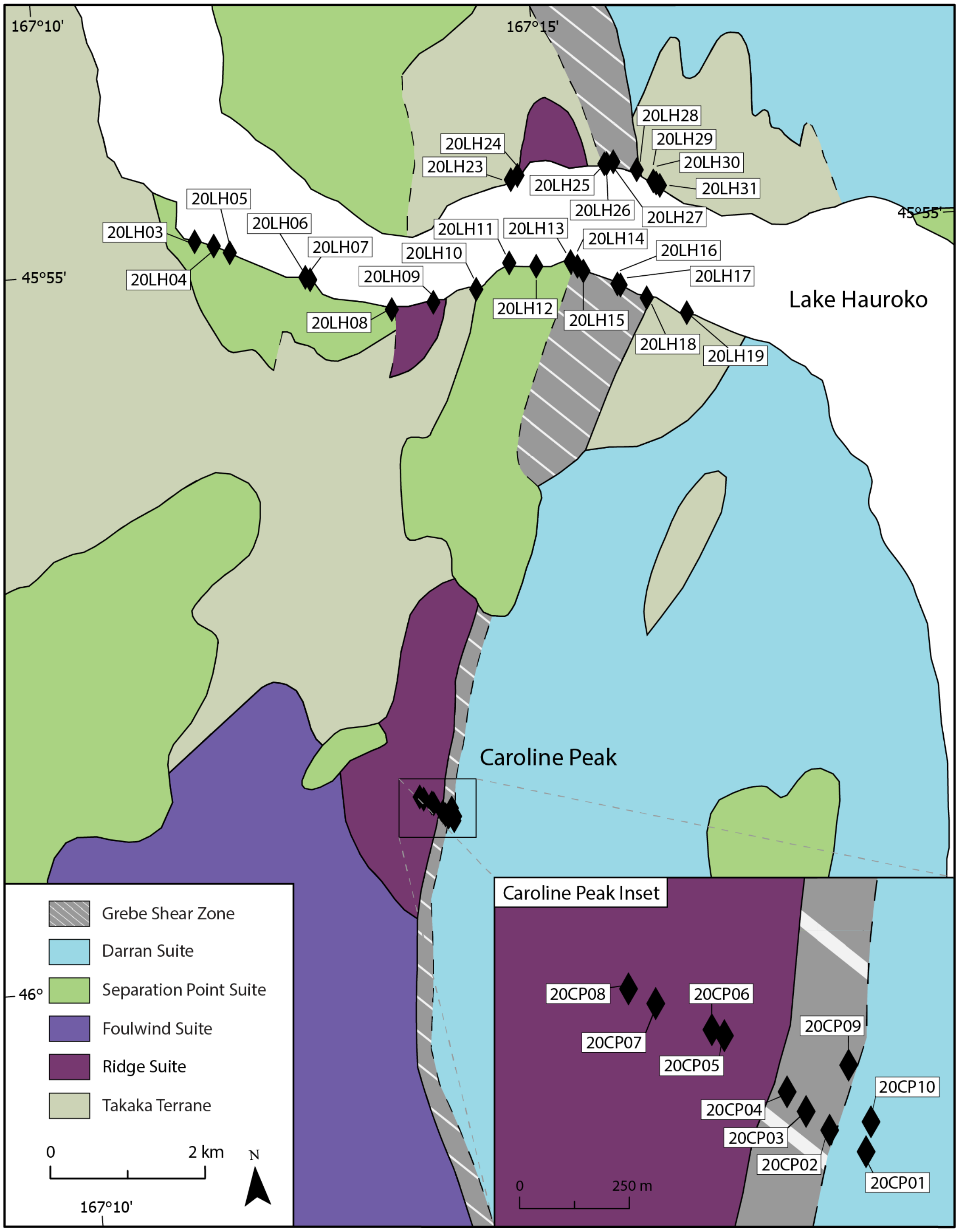

Figure 9. A map of the study area where the GSZ was encountered at Lake Hauroko and Caroline Peak. Formation information including age, location, and suite from Turnbull et al., 2010. Dashed lines represent fault contacts.

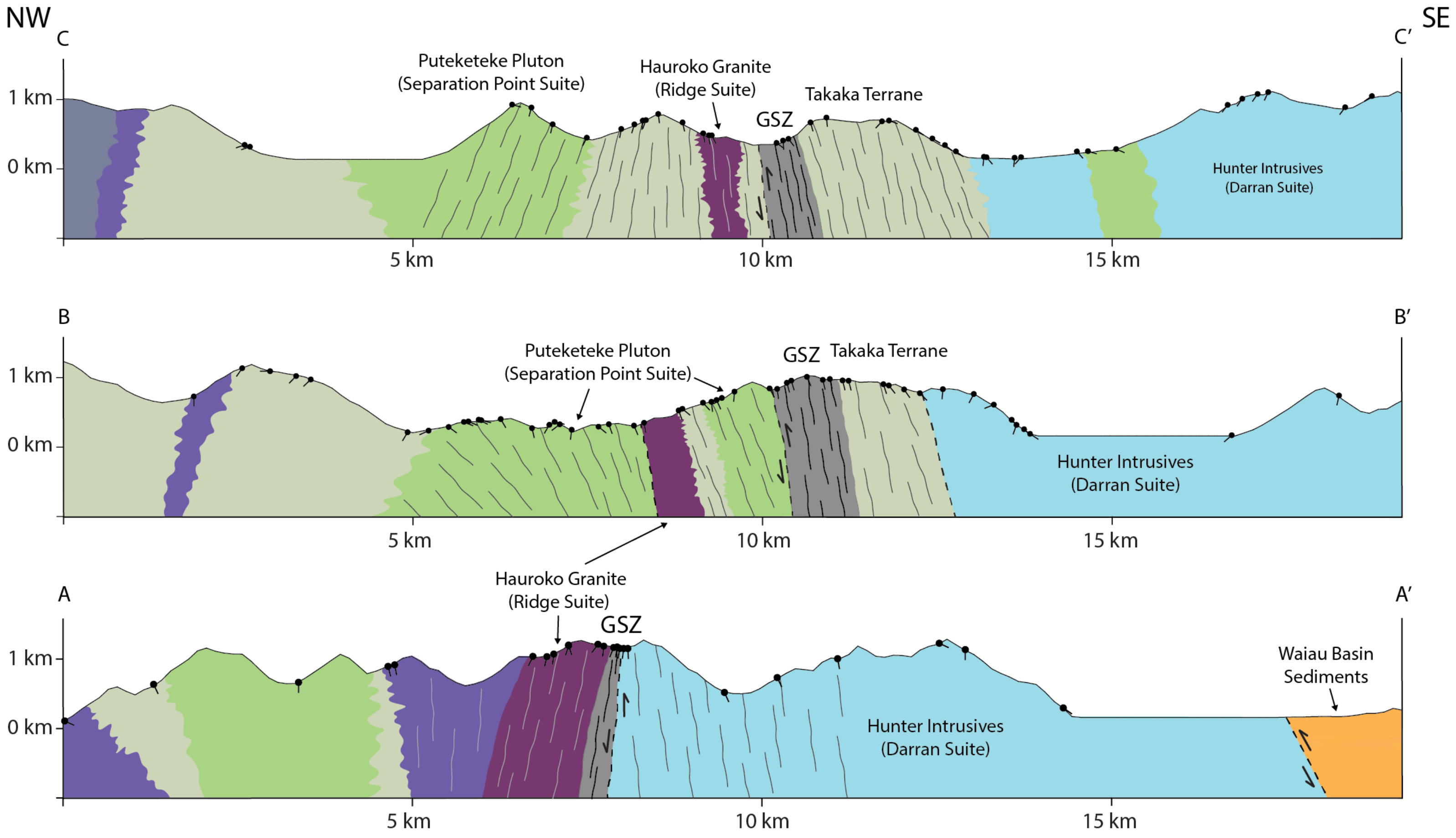

Figure 10. Cross sections depicting subsurface geology of transects A-A' (Caroline Peak), B-B' (Lake Lauroko South Shore), and C-C' (Lake Hauroko North Shore). Ball and tick symbols represent planar measurements used to create the cross-sections. Cross-section locations can be found in Figure 6.

4.1.1 Definition of Fabrics

At Lake Hauroko, several generations of igneous rock intrusions and deformations occurred, as evident by the presence of cross cutting, variably deformed, folded dikes in and around the shear zone. The GSZ has been characterized as the boundary between the inboard and outboard Median Batholith of Fiordland. Therefore, we chose to evaluate each side of the shear zone separately. Based on field observations of cross-cutting relationships among features and fabrics, a sequence of events was discerned for each side of the GSZ (Figure 11). This determination is important in ensuring that fabrics are being compared equitably across the shear zone.

The dominant foliation (S_{Grebe}) within the GSZ is mylonitic and parallels the axial planes of tight, intrafolial folds of metasedimentary layering and tonalitic dikes. This foliation dips steeply to the east. Mineral stretching lineations defined by aligned grains of quartz and biotite cluster into two groups: lineations that plunge moderately to the south and southeast, and those that plunge moderately to the east (Figure 12). Minor folds of the mylonitic foliation plunge gently to the north and have axial planes that dip steeply to the west.

The dominant foliation located west of the GSZ is a penetrative schistosity (S_2^W) that parallels the axial planes of tight, intrafolial folds (F_2^W) of metasedimentary layering and minor tonalite dikes (S_1^W). S_2^W is defined by flattened aggregates of quartz, plagioclase, and biotite in mafic schist and mainly plagioclase and biotite in tonalite. It dips moderately to the east and southeast. In a few places, it displays a weak quartz-biotite mineral stretching lineation (L_2^W) that plunges moderately to the east and southeast (Figure 12). Open folds of S_2^W (F_3^W) plunge moderately to the north, northeast, and southwest. These three structures define three main deformational events in the section located the west of the GSZ. All of these predate the formation of the shear zone (Figure 11). Similarly, the dominant foliation located east of the GSZ is a penetrative schistosity (S_2^E) that parallels the axial planes of tight, intrafolial folds (F_2^E) of metasedimentary and metaigneous layering (S_1^E). S_2^E is defined by flattened aggregates of biotite and dips moderately to the southeast. Isoclinal folds plunge steeply to the north and have axial planes that dip moderately to the north-northeast, suggesting that they may be related to the formation of S_{Grebe}.

Observations at Caroline Peak showed a similar pattern in the orientation of foliations, where foliations on either side of the GSZ are approximately parallel to the boundaries of the shear zone (Figure 12). Other similarities observed included the intrusion of post-kinematic granitic dikes and brittle overprint, which provides additional information regarding shear zone reactivation. Caroline Peak samples were generally more coarse-grained than Lake Hauroko samples, resulting in the preservation of lithology and sense of shear indicators. Therefore, in this context these samples were primarily used to describe the mineralogy of the shear zone.

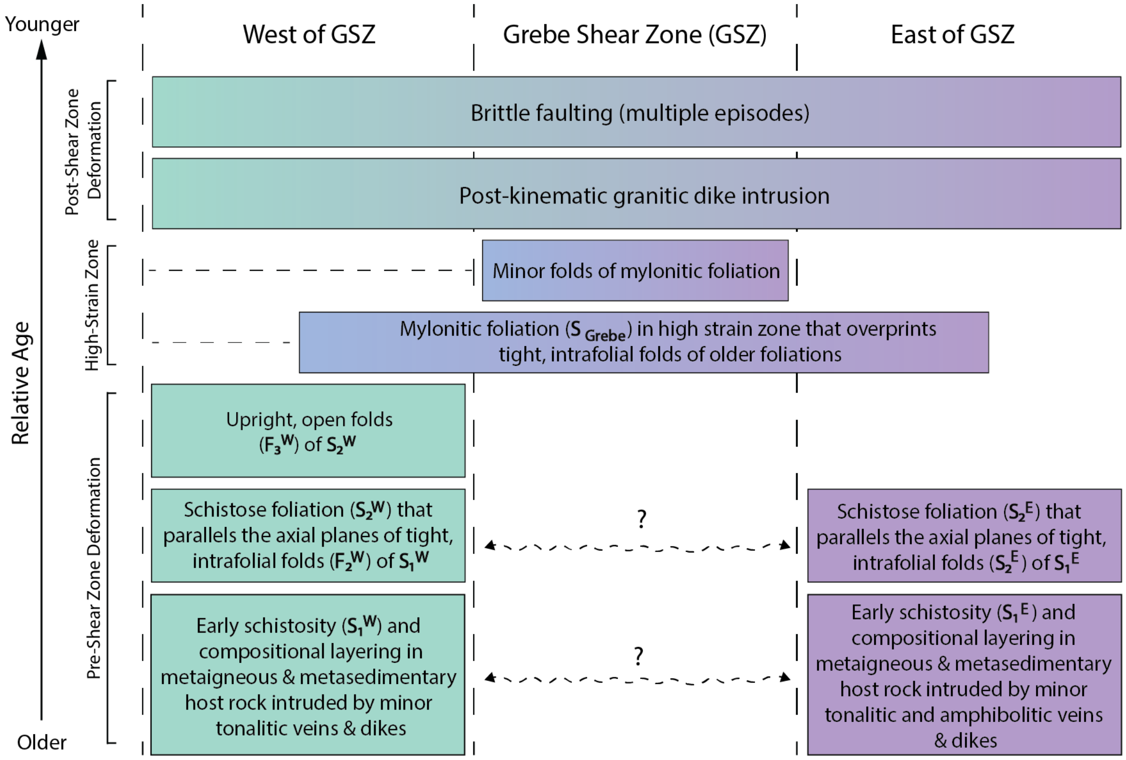

Figure 11. A sequence of events discerned of the area surrounding the southern GSZ by using cross-cutting relationships of structures observed in the field. The connection between pre-shear zone deformational events cannot be definitively made due to overprinting of mylonitic foliation, however it is possible that the protolith on either side of the GSZ is the same. Comprehensive geochemical analysis would need to be conducted to draw this conclusion. Though the shear zone represents the divide between the inboard and outboard Median Batholith, it may not always behave as an absolute boundary.

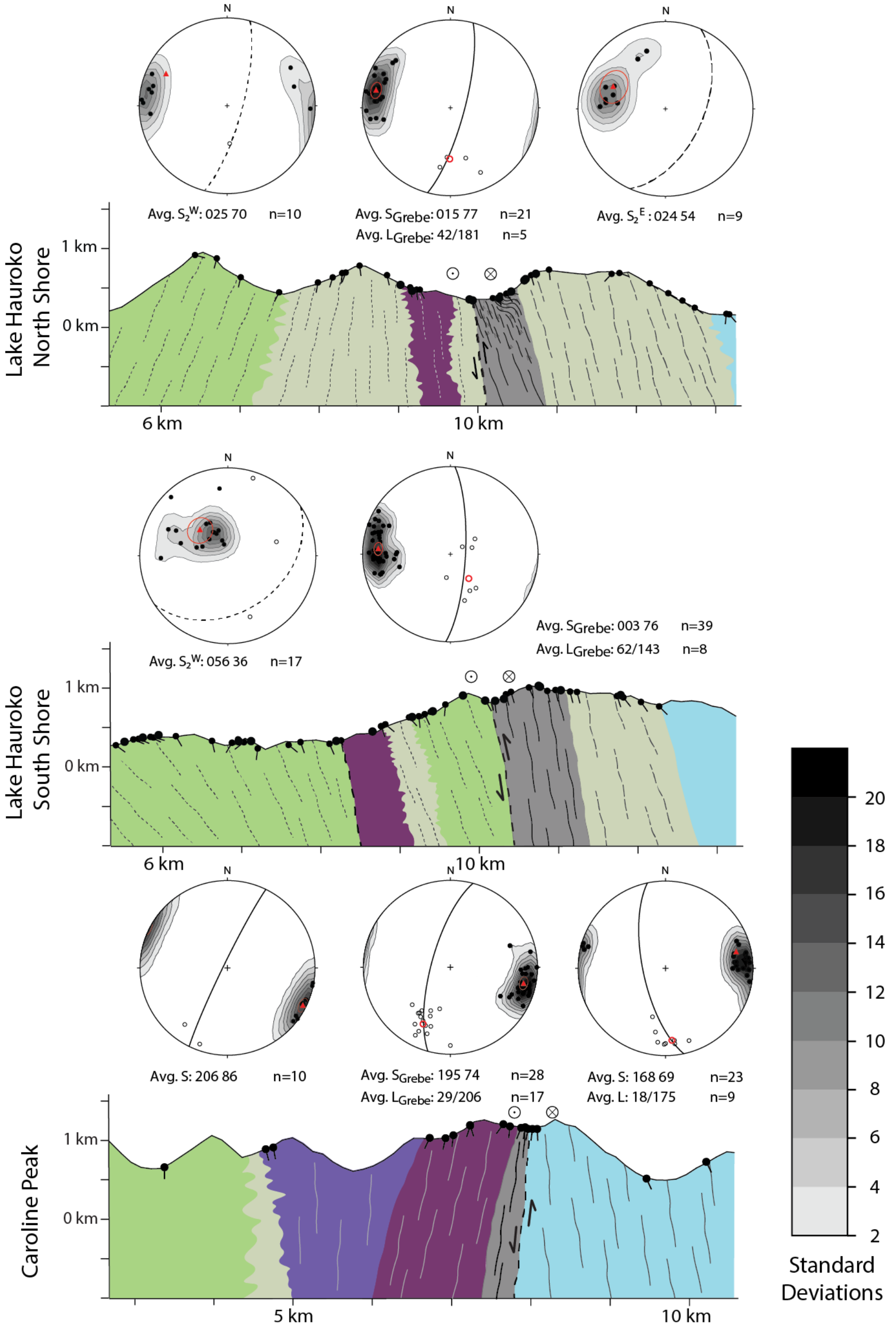

Figure 12. Cross sections zoomed to the GSZ at Lake Hauroko and associated stereonets showing average foliation and lineation measurements. Poles to foliations are plotted and contoured using Kamb contouring on either side of the GSZ. The red triangle and circle represent the mean vector of each population, the closest measured foliation to this calculation was used as the average. Mineral stretching lineations are shown as hollow circles, with average lineations shown in red.

4.1.2 The GSZ at Lake Hauroko, North Shore

On the north shore of the lake, the GSZ is bordered by a cataclastic fault zone within Paleozoic basement rock and portions of the Hauroko Granite (Ridge Suite) to the west, and exposures of basement rock to the east. The dominant shear zone foliation strikes to the north-northeast (350-041°) and dips steeply (66-86°) to the east-southeast. The shear zone is composed of interlayered schist and protomylonite-mylonitic foliation that deforms older layering. On the western side of the shear zone, shear bands exhibiting sinistral top-to-the-southwest shear senses were observed in the schist. The shear zone foliation includes intrafolial folds of granitic orthogneiss. A fault zone with cataclastic texture was observed on the western edge of the shear zone cutting all features.

In thin section, foliation is primarily defined by clinozoisite-rich domains with chlorite tails in a matrix of plagioclase and minor hornblende (Figure 13). The primary mineral assemblage is consistent with the retrogression of an amphibolite facies metamorphic mineral assemblage, as indicated by the growth of chlorite at the expense of clinozoisite and amphibole. Evidence of plagioclase altering to white mica occurs within the cleavage planes of feldspar, which is also indicative of retrogression.

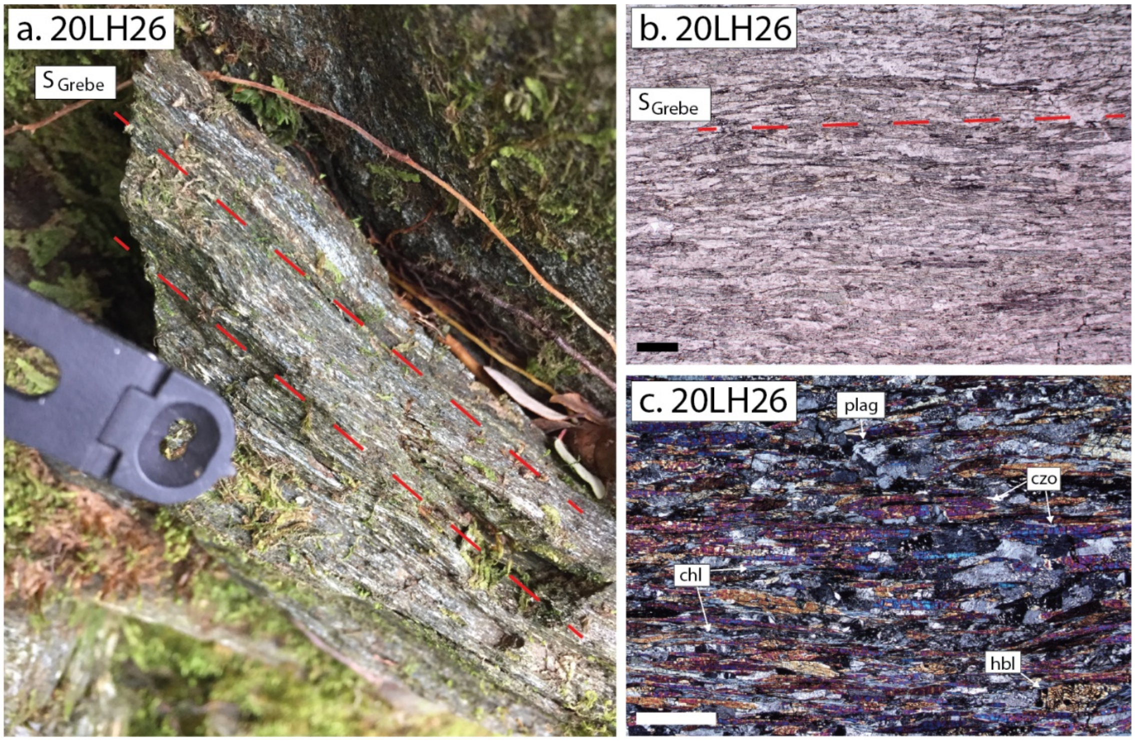

Figure 13. Photographs of mylonitic foliation (S_{Grebe}) at station 20LH26 on Lake Hauroko at outcrop scale (a) and in thin section (b). Mineral assemblage including plagioclase (plag) + chlorite (chl) + hornblende (hbl) + clinozoisite (cz) shown in (c). Scale bars in b and c are 1 mm.

4.1.4 The GSZ at Lake Hauroko, South Shore

On the south shore, the GSZ is bordered to the west by the Puteketeke Pluton (Separation Point Suite) and a zone of cataclastic faulting within metaigneous and metasedimentary Paleozoic rock to the east. The dominant shear zone foliation (S_{Grebe}) is characterized by interlayered quartzo-feldspathic mylonite and biotite-rich schist. The foliation strikes to the north-northeast (344-025°) and dips steeply (50-88°) to the east. Mineral lineations plunge moderately-steeply (49-77°) to the east-southeast (058-163°) It is cut by variably deformed granite, amphibolite dikes, and reactivated by brittle faults.

Biotite S-C type shear bands were observed at outcrop scale at stations 20LH14 and 20LH26, exhibiting sinistral top-to-the-southwest sense of shear.

In thin section, S_{Grebe} shows an alignment of biotite, hornblende, and chlorite with minor epidote defining foliation in a matrix of primarily quartz, plagioclase feldspar, and microcline (Figure 14). Minor minerals include garnet, titanite, and magnetite. Quartz grains exhibit undulose extinction and have sub-grains. Lattice preferred orientation of quartz grains was observed when viewed with a quartz accessory plate. Feldspar grains appear predominantly brittlely deformed with some samples containing deformation lamellae (20LH14D, 20LH15, and 20LH16C), indicative of relatively low temperature of deformation (<400°C) (Passchier & Trouw, 2005).

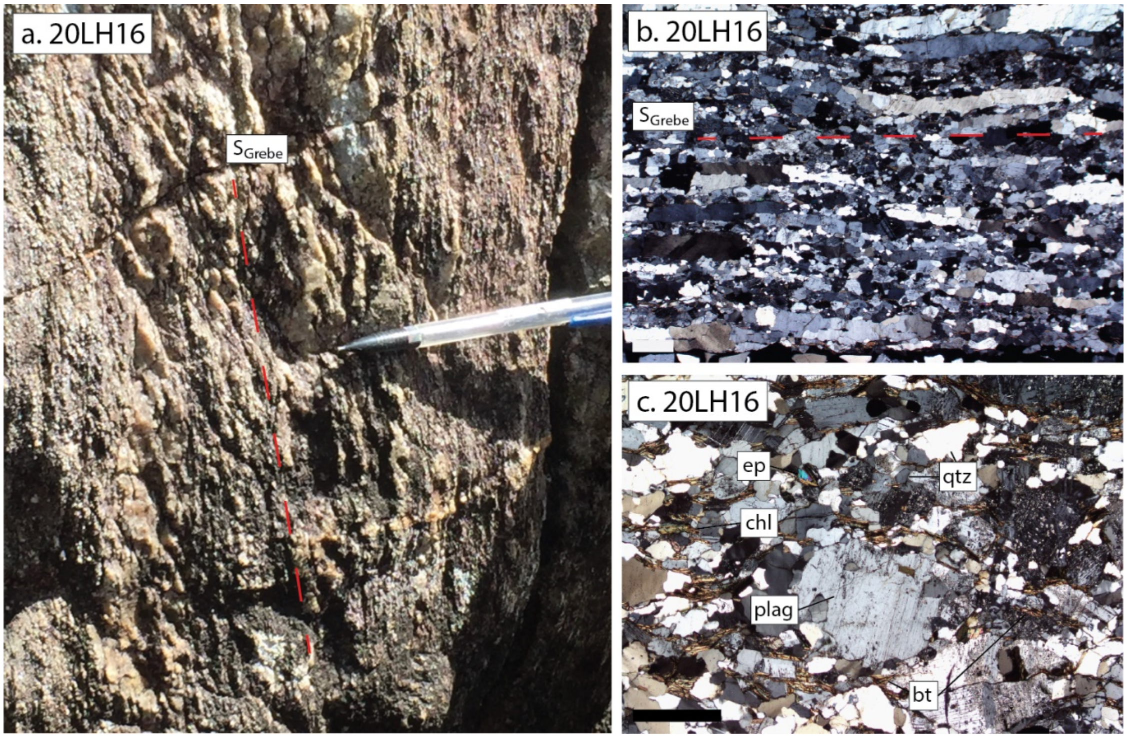

Figure 14. Photographs of mylonitic foliation (S$_{Grebe}$) at 20LH16 on Lake Hauroko at outcrop scale (a) and in thin section (b). Mineral assemblage including plagioclase (plag) + chlorite (chl) + quartz (qtz) + epidote (ep) shown in (c). Scale bars in b and c are equal to 1 mm.

4.1.5 The GSZ at Caroline Peak

At Caroline Peak, the GSZ is bordered by the Hauroko Granite to the west, and a zone of cataclastic deformation within dioritic plutons to the east. Here, the shear zone displays mylonitized granitic rock with a foliation that strikes to the south-southwest (169-210°) and dips steeply (56-87°) to the west. Mineral lineations are primarily composed of stretched quartz and feldspars and generally plunge gently to the southeast. The entire shear zone is cross-cut by coarse-grained biotite-granite pegmatite dikes with varying degrees of fabric development. An epidotized fault zone with cataclastic texture and chatter marks exhibiting apparent normal motion was observed on the eastern edge of the shear zone at station 20CP02. Additionally, sinistral top-to-the-northeast shear sense within the mylonite was indicated by asymmetric strain shadows on plagioclase augen viewed in the XZ plane at station 20CP03.

In thin section, the shear zone foliation shows an alignment of biotite and plagioclase. The mineral assemblages include biotite, plagioclase feldspar, quartz, hornblende, and clinozoisite (Figure 15). Quartz exhibits undulose and checkerboard extinction and, in some places, has sutured boundaries, indicative of grain boundary migration. Lattice preferred orientation of small quartz grains was observed when viewed with a quartz accessory plate. Plagioclase appears primarily twinned and fractured with minor deformation lamellae and pressure shadows composed of biotite. In sample 20CP04, hornblende appears ragged and inundated with quartz inclusions, suggesting that it began reacting out during retrograde metamorphism (Figure 13). This, along with the presence of metamorphic biotite and clinozoisite in aligned biotite domains, suggests that this was an amphibolite facies mineral assemblage that underwent retrogression to greenschist facies conditions.

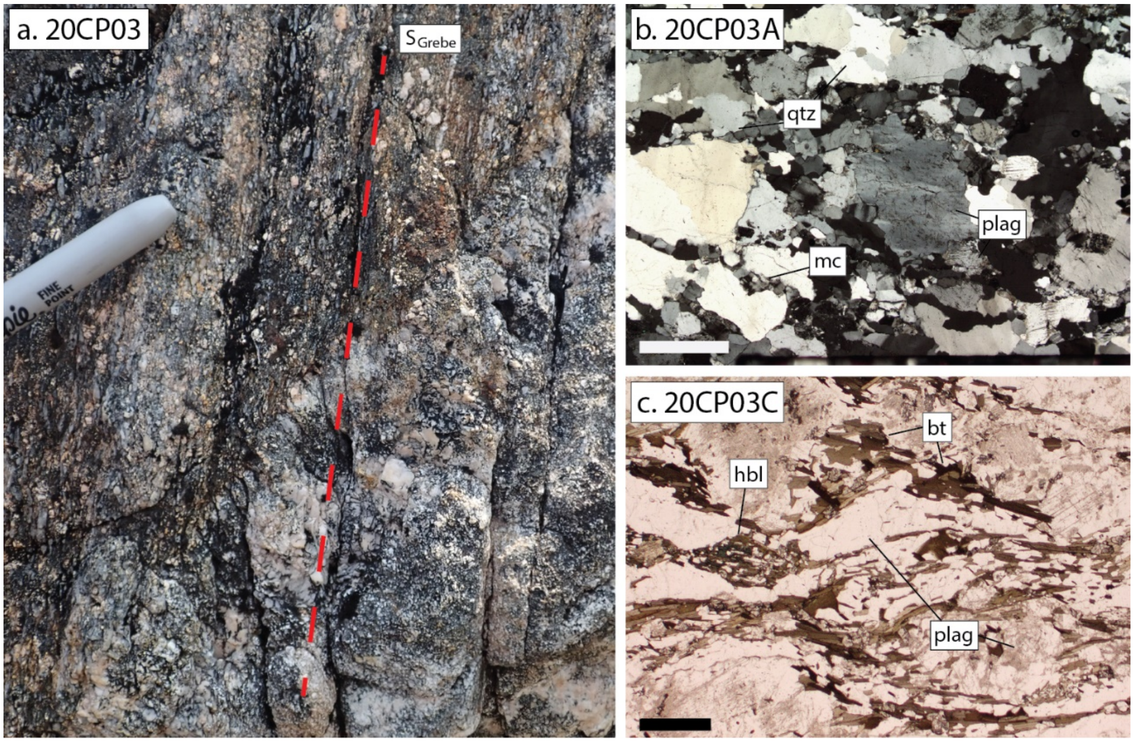

Figure 15. Photographs of shear zone fabric (S$_{Grebe}$) at station 20CP03 at Caroline peak at outcrop scale (a) and in thin section (b & c). General microstructure of GSZ including quartz (qtz) + plagioclase (plag) + microcline (mc) in (b); relic hornblende (hbl) with quartz inclusions and biotite (bt) coronas around plagioclase grains in (c). Scale bars in b and c are equal to 1 mm.

4.1.6 Surrounding Fabric

In order to assess a metamorphic regime across the shear zone, thin sections from samples outside of the shear zone were also evaluated. Thin sections were observed to the east of the GSZ from Caroline Peak and to the west of the GSZ from Lake Hauroko and Caroline Peak.

East of the GSZ

At Caroline Peak, foliation is defined by aligned biotite and chlorite in a matrix of quartz, plagioclase, microcline, and some amphibole. Quartz exhibits undulose extinction and some deformational twinning of plagioclase was observed. The presence of amphibole and chlorite within foliation domains is indicative of amphibolite facies pressure and temperature conditions that underwent retrogression to greenschist facies conditions.

West of GSZ

Along the north shore of Lake Hauroko, foliation is defined by aligned biotite and chlorite in a matrix of primarily quartz, plagioclase, and hornblende. Larger quartz grains exhibit chessboard extinction and have interlocking grain boundaries, indicative of grain boundary migration. Minor myrmekitic texture was observed and is indicative of higher temperature deformation. Metamorphic biotite forms pressure shadows on clusters of quartz and plagioclase, suggesting that the rock underwent amphibolite metamorphic facies conditions and was retrogressed to greenschist facies conditions. On the south shore, foliation was indistinguishable in thin section, however evidence of higher metamorphic grade minerals was observed, including chlorite and garnet. Quartz exhibits undulose extinction and has interlocking and amoeboid grain boundaries, creating sub-grains. Plagioclase grains appear fractured and have some deformation lamellae. Additionally, epidote is observed growing on cleavage planes of plagioclase, suggesting that the rock experienced retrogression to greenschist temperature and pressure conditions.

At Caroline Peak, foliation is defined by aligned biotite, hornblende, and minor epidote in a matrix of primarily quartz and plagioclase. Quartz exhibits undulose and chessboard extinction and hornblende inclusions are present within plagioclase aggregates. Plagioclase appears fractured with some deformation lamellae. The presence of relic hornblende is indicative of retrograde metamorphism from amphibolite to greenschist facies conditions.

4.2 Kinematics and Finite Strain Results from the Grebe Shear Zone

The purpose of conducting finite strain analysis is to compare fabric intensity and the shape and orientation of fabric ellipsoids in and around the GSZ to aid our kinematic analysis and to evaluate if the deformation is compatible with transpression. In addition, we used the data to evaluate a strain gradient across the shear zone to determine how older foliations were affected by shear zone deformation and the degree to which the deformation is localized.

4.2.1 Strain Intensity and Fabric Ellipsoid Results

Finite strain analysis was conducted on feldspar aggregates in samples 20CP03C, 20LH14A, 20LH14C, 20LH14D, and 20LH15 from within the shear zone (Figure 9). Samples outside of the shear zone that were analyzed include 20CP01, 20LH11A, 20LH23, and 20LH24C (Figure 9). These samples were chosen because feldspar grains can be differentiated from surrounding mineralogy in hand sample and the aggregates are large enough to manually trace using *EllipseFit.* At least three and up to seven faces were analyzed for each sample depending on how they were cut. For each sample face, a minimum of 30 to a maximum of 60 ellipses were selected for the calculation of the strain ellipse. Comprehensive ellipse and ellipsoid analysis data can be found in Appendix B (pg. 84).

The Nadai-Hsu plots (Figure 16) show results of finite strain analysis in (a) feldspars in hand sample and (b) in quartz in thin section with associated 95% confidence intervals. The plot allows us to compare relative strain intensities and the shapes of fabric ellipsoids among our samples. Vollmer (2010) noted that this particular method of displaying data is associated with distortion at low strains, however we are using it with the caveat that the strain intensities found in this analysis are likely not measurements of true strains. Instead, we aimed to observe changes in relative strain intensity across the shear zone. This is because we chose to measure strain in feldspars due to their availability in our samples which, in thin section, have not widely exhibited evidence of dynamic recrystallization. In general, the shape of the fabric ellipsoids within the GSZ exhibit oblate to plane strain. Oblate fabric ellipsoids reflect flattening strains and are compatible with a component of shortening across the GSZ (Dewey et al., 1998). The relative strain intensity measured using feldspar is generally low, however there is some minor variability from Caroline Peak to Lake Hauroko, with Caroline Peak exhibiting the highest strain with respect to our field area. Some minor variability in the relative strain intensity is also seen on either side of the GSZ, with generally higher strain recorded by metasedimentary rock located east of the shear zone. The largest errors associated with this analysis were in variability in the X direction of the fabric ellipsoid (Table 2). This variability likely reflects the low strain intensity recorded by feldspar.

Nevertheless, the orientations generally scatter around the same orientations as observed in the field.

Finite strain analysis was also conducted on quartz in two samples in thin section (20LH14D and 20LH15). These samples were chosen for this analysis because three thin sections from different faces were made for each sample, which allows for a finite strain ellipsoid to be calculated using this same method. The purpose of conducting this analysis on quartz was to compare relative strain recorded by the two minerals and to determine if low strains in feldspar can be attributed to the higher degree of dynamic recrystallization in quartz. When compared with feldspar, quartz exhibits higher relative strain intensity. However, the confidence intervals are too large to make a definitive comparison.

A (Maximum)

Sample	N	Length (Å)	95% CI	Trend	95% CI	Plunge	95% CI	Alpha 95% CI
20CP01	5	1.377	0.057	155.45	3.27	0.36	7.03	7.63
20CP03	5	1.294	0.057	145.95	19.92	58.44	18.44	21.04
20LH11A	5	1.161	0.084	100.7	24.7	9.25	9.18	25.87
20LH14A	5	1.253	0.059	175.14	49.88	72.14	11.79	17.22
20LH14C	3	1.413	0.059	255.25	6.06	47.71	6.08	6.91
20LH14D	7	1.118	0.031	78.2	71.71	72.57	25.38	39.9
20LH15	5	1.225	0.065	339.28	4.67	35.26	11.71	11.88
20LH23	4	1.324	0.062	264.33	28.62	62.42	4.92	14.44
20LH24C	3	1.247	0.069	142.13	80.89	80.8	34.02	37.59
B (Intermediate)								
20CP01	5	1.061	0.033	249.47	63.76	84.83	4.72	7.8
20CP03	5	1.163	0.043	349.51	6.92	29.38	19.84	20.94
20LH11A	5	0.991	0.056	9.23	26.18	8.95	23	33.38
20LH14A	5	1.078	0.053	15.11	4.68	16.85	13.99	17.24
20LH14C	3	0.999	0.39	111.48	7.16	36.24	6.46	7.58
20LH14D	7	1.059	0.034	346.48	15.03	0.54	36.64	39.91
20LH15	5	1.02	0.039	152.58	8.03	54.56	11.69	11.95
20LH23	4	1.043	0.052	168.98	10.96	2.79	11.91	15.46
20LH24C	3	1.128	0.055	359.51	5.87	7.34	35.3	37.64
C (Minimum)								
20CP01	5	0.684	0.022	65.42	3.05	5.16	3.69	4.28
20CP03	5	0.662	0.018	253.52	3.14	10.5	2.38	3.44
20LH11A	5	0.869	0.054	235.91	77.61	77.07	21.19	27.85
20LH14A	5	0.74	0.017	283.36	3.55	5.75	2.92	4.11
20LH14C	3	0.708	0.026	7.09	5.09	18.7	3.46	5.59
20LH14D	7	0.845	0.021	256.31	7.12	17.43	4.18	7.25
20LH15	5	0.8	0.022	247.04	4.34	3.17	3.21	5.19
20LH23	4	0.724	0.029	77.53	10.84	27.41	3.62	9.96
20LH24C	3	0.711	0.026	268.8	4.82	5.53	3.99	5.52

Table 2. Finite strain ellipsoid results (axes lengths and orientations) and associated 95% confidence intervals. N represents the number of sample faces included in the analysis. The alpha 95% CI represents the angular error.

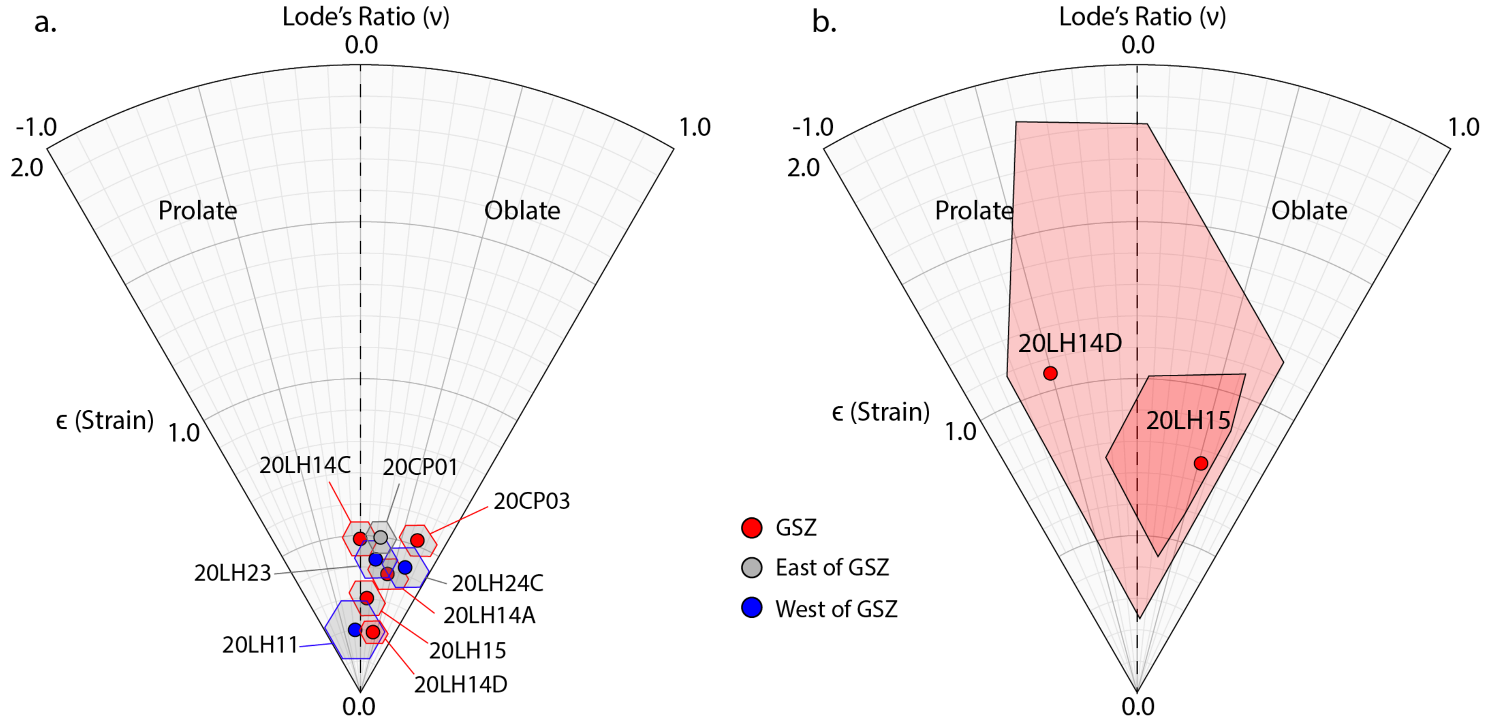

Figure 16. Nadai-Hsu plot of finite strain ellipsoids of feldspar aggregates in hand sample (a) and quartz ribbons in thin section (b) with 95% CI's, where lateral deviation from the center of the plot (v = 0.0) describes the shape of the fabric ellipsoid, and vertical position describes relative strain intensity (ε). Samples from the GSZ are shown in red and generally exhibit oblate to plane strain with varying intensity in feldspars. In feldspars, samples to the east of the GSZ exhibit oblate strain with higher strain intensity than samples to the west. One sample (20LH11) was analyzed from the west side of the GSZ and exhibits plane strain, however the CI for this sample can place it in either the prolate or oblate domain. In general, strain intensity at Caroline Peak is greater than at Lake Hauroko. Additionally, the strain intensity exhibited in quartz is larger than that in feldspars, however the 95% CI's for the quartz ellipsoids overlap those of the feldspar ellipsoids, so a definitive correlation cannot be made

4.2.2 Rotation of Structures in Response to Shear Zone Formation

Fabric deflection and rotation of extensional and contractional features are common consequences of shear zone formation (Sanderson & Marchini, 1984). The orientation of the foliations around the GSZ show an apparent deflection in where foliations progressively steepen towards vertical as they approach the boundaries of the shear zone (Figure 17). This pattern appears regionally when including foliation measurements collected from previous studies (Turnbull et al., 2010), implying that the formation of the shear zone influenced the orientation of these fabrics and suggesting that deformation was dominated by simple shearing.

A distinct relationship exists between the angle of contractional and extensional structures and the boundaries of transpressional shear zones (Sanderson & Marchini, 1984). Sanderson and Marchini (1984) noted that folds and thrusts initiate at low angles (<45°) with respect to the shear zone boundaries, whereas veins and dikes initiate at higher angles (>45°) (Figure 18). Axial planes of isoclinal folds in rocks to the east of the shear zone (station 20LH31) are oriented nearly parallel to the shear zone boundary (Figure 19). Therefore, the low angle of the axial planes of these folds with respect to the shear zone boundary (approximately 25° on the north shore of Lake Hauroko) is consistent with a component of shortening across the shear zone during deformation.

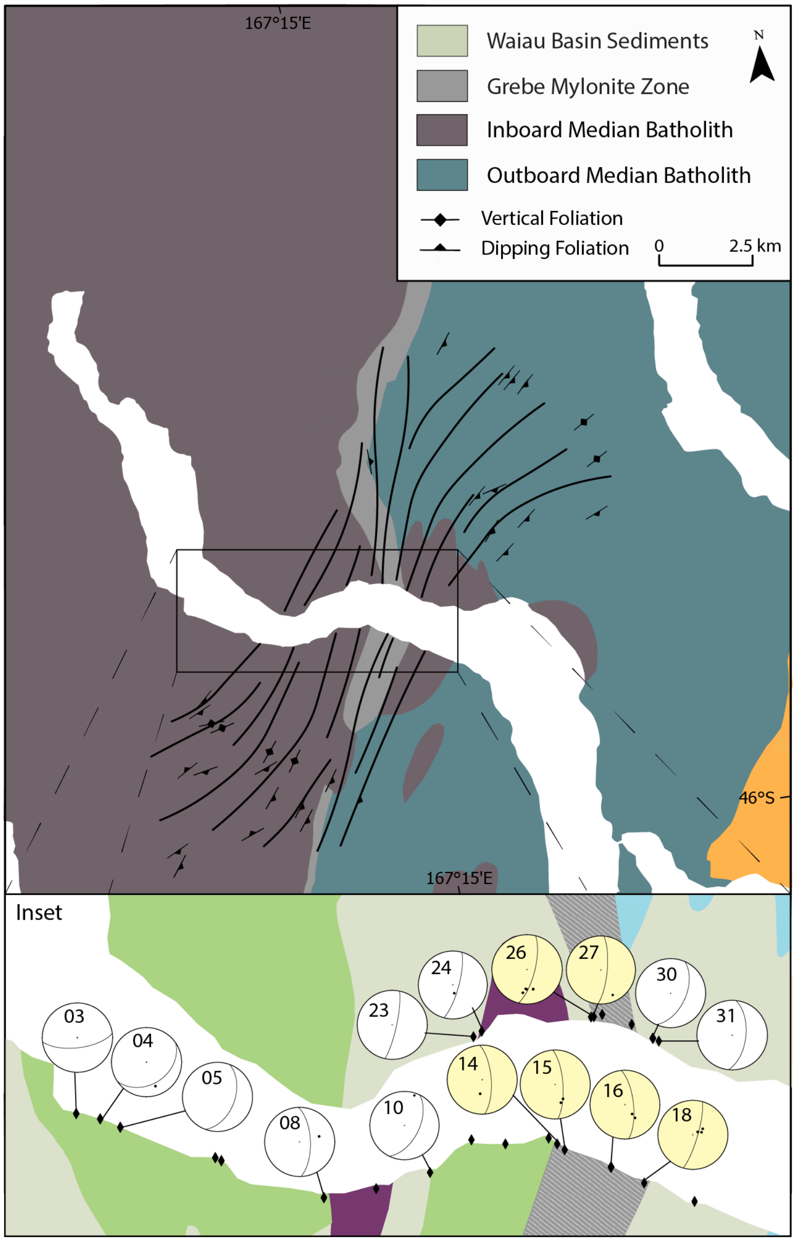

Figure 17. Foliation deflection around Lake Hauroko. Stereonets show average foliation plane and lineations for each station (denoted by the last two numbers of the station name for readability). Foliations projected on the map are from previous studies (Turnbull et al., 2010).

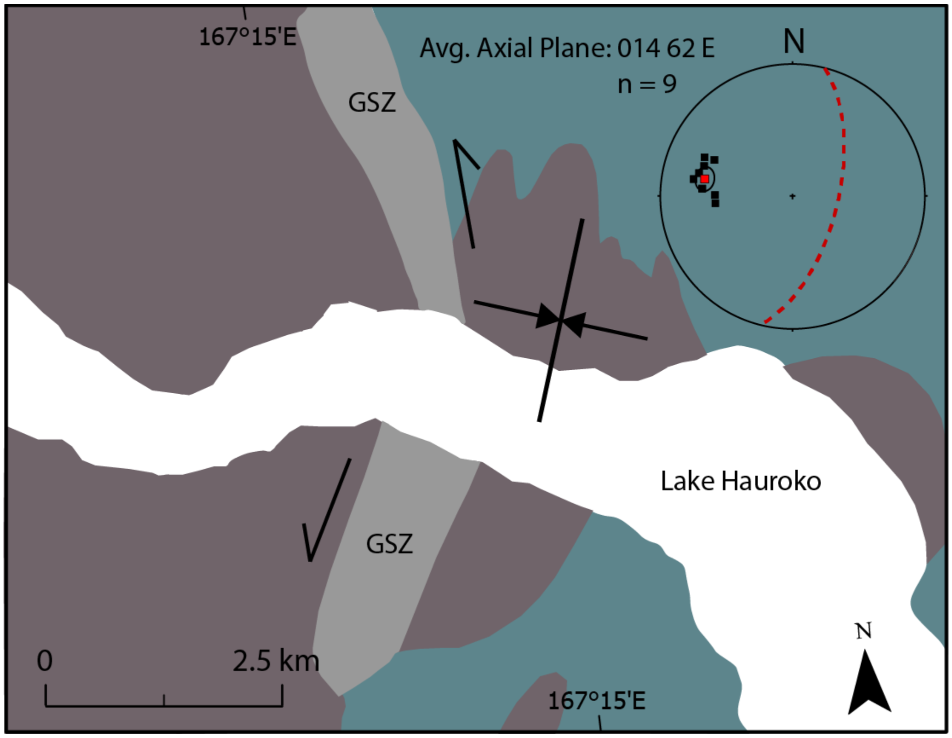

Figure 18. Orientation of isoclinal folds near Lake Hauroko with respect to the shear zone boundary. The red dashed line on the stereonet represents the average axial plane orientation, lines are poles to axial planes.

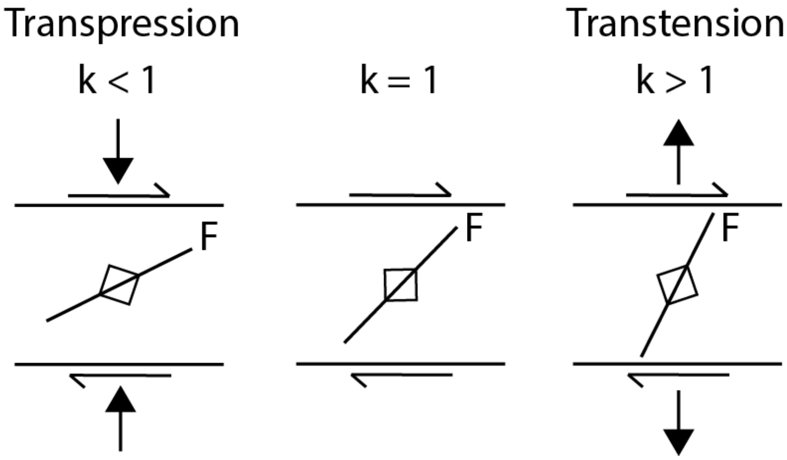

Figure 19. Diagram adapted from Sanderson et al. (1984) illustrating the relationship between shear zone boundaries and fold initiation in transpression, pure shearing, and transtension.

4.2.2 Shear Sense of Ductile Fabrics

To further characterize the shear zone in three dimensions, we observed sense of shear indicators in thin sections oriented parallel, normal, and/or oblique to shear zone fabrics. These included faces representing the XZ plane (normal to foliation, parallel to lineation), YZ plane (parallel to both foliation and lineation), and/or faces oriented oblique to the XZ and YZ planes (denoted as "trim block") (Figure 20). The purpose of this analysis is to view asymmetry in samples with respect to the observed maximum stretching direction, which provides additional insight into the behavior of strain during deformation. Samples analyzed within the shear zone include 20CP03A, 20CP03C, 20CP04, 20LH14A, 20LH14C, 20LH14D, 20LH15, 20LH16B, 20LH16C, and 20LH26 Tables 3 & 4).

Caroline Peak

Samples 20CP03A, 20CP03C, and 20CP04 from Caroline Peak were observed in thin section. Asymmetric shear sense indicators were observed in all three orientations (XZ, YZ, and trim block faces) and include biotite S-C type shear bands and plagioclase sigma and delta clasts with quartz and biotite pressure shadows (Figure 21) (Table 3). Asymmetric shear bands are defined by aligned blades of brown biotite ± epidote and exhibit a dominant sinistral component of shear. Large aggregates of quartz and feldspar have asymmetric pressure shadows of biotite and epidote also exhibiting mostly sinistral shear. Some pressure shadows on equant aggregates are symmetrical, however elongate aggregates tend to be asymmetric. Back-rotated feldspar clasts with quartz pressure shadows growing from its' broad faces were observed in sample 20CP04-1 (Figure 21). The highest degree of asymmetry was generally observed on the XZ plane, however both symmetrical and asymmetrical structures were observed on faces oriented both normal and oblique to lineation (Table 4).

Lake Hauroko

At Lake Hauroko, samples 20LH14A, 20LH14C, 20LH14D, 20LH15, 20LH16B, 20LH16C, and 20LH26 were observed in thin section. Asymmetric shear sense indicators observed include biotite shear bands, feldspar sigma clasts with quartz and biotite strain shadows, mica and amphibole fish, and lattice preferred orientation of quartz (Figure 21) (Table 3). The degree of asymmetry between different faces of the samples varied, with most asymmetric sense of shear indicators being observed on the XZ face. However, samples 20LH14C and 20LH15 were observed to have the most asymmetric sense of shear indicators on the YZ and oblique faces respectively. Specifically, sample 20LH15 exhibited a dominant right-lateral sense of shear on the oblique face, whereas the XZ and YZ faces had the most symmetrical structures (Table 4).

Sample	Plane	Shear Sense	Strain Shadows (On Plagioclase)	Shear Bands (Biotite)	Mineral Fish	LPO (Quartz)
20CP03A	XZ	L	X (qtz + bt)	-	-	-
20CP03C-1	XZ	L	X (qtz + bt)	X	-	-
20CP03C-2	YZ	L	X (qtz + bt)	-	-	-
20CP04-1	XZ	L	X (qtz + bt)	X	-	-
20CP04-2	YZ	L	X (qtz + bt)	X	-	-
20CP04-3	O	L	X (qtz + bt)	X	-	-
20LH14A	XZ	R	X (bt)	-	X (amph)	-
20LH14C-1	XZ	R	X (bt + ep)	X	-	-
20LH14C-2	YZ	L	X (bt + ep)	X	-	-
20LH14D-1	XZ	L	X (qtz + bt)	-	-	-
20LH14D-2	YZ	S	X (qtz + bt)	-	-	-
20LH14D-3	O	L	X (qtz + bt)	-	-	-
20LH15-1	XZ	S	-	-	-	X
20LH15-2	YZ	L	-	-	-	-
20LH15-3	O	R	X (qtz + bt)	X	-	-
20LH16B-1	XZ	R	X (qtz + bt)	X	-	X
20LH16B-2	YZ	NO	-	-	-	-
20LH16B-3	O	NO	-	-	-	-
20LH16C-1	XZ	L	X (qtz + bt)	-	-	-
20LH16C-2	YZ	R	X (qtz + bt)	-	-	-
20LH16C-3	O	R	-	-	-	-
20LH26-1	XZ	R	-	X	X (wm)	-
20LH26-3	O	L?	-	X	-	-

Table 3. Thin section samples from the GSZ and their orientations with respect to the X, Y, and Z directions of the finite strain ellipsoid, with O indicating that the section is oblique to the XZ and YZ planes. Sense of shear is recorded for with respect to each section as L (left-lateral), R (right-lateral), S (symmetric), or NO (not observed) based on structures observed. Minerals abbreviations include quartz (qtz), biotite (bt), epidote (ep), amphibole (amph), and white mica (wm). Dashes indicate that specific sense of shear indicators were not observed.

Sample	Plane	L	R	Total	Geographic Interpretation
20CP03A	XZ	10	3	13	S-N
20CP03C	**XZ**	9	4	**13**	S-R
	YZ	11	1	12	
20CP04	**XZ**	12	3	**15**	S-R
	YZ	8	2	10	
	O	6	3	9	
20LH14A	XZ[1]	0	12	12	S-R
20LH14C	XZ	2	5	7	S-N
	YZ	16	1	**17**	
20LH14D	**XZ**	6	3	**9**	S-N
	YZ	1	0	1	
	O	3	2	5	
20LH15	XZ	7	6	13	S-N
	YZ	8	6	14	
	O[2]	1	16	**17**	
20LH16B	**XZ**	1	2	**3**	D-N[3]
	YZ	0	0	0	
	O	1	0	1	
20LH16C	**XZ**	5	3	**8**	S-N
	YZ	0	5	5	
	O	0	1	1	
20LH26	**XZ**	0	5	**5**	S-R
	O	1	0	0	

Table 4. Asymmetric sense of shear indicators counted in samples. L represents left-lateral (sinistral), R represents right-lateral (dextral). Bolded planes designate the maximum asymmetry plane observed in samples with more than one thin section. Geographic interpretations are as follows: S-N indicates sinistral with a slight normal component, S-R indicates sinistral with a slight reverse component, D-N inidcates dextral with a slight normal component, and D-R indicates dextral with a slight reverse component. [1] [2] Thin sections from overturned surfaces, so that when dextral is translated into geographic coordinates, it becomes sinistral with a minor reverse component[1] or

sinistral with a minor normal component[2]. [3]Shear sense observed is dextral, however the number of shear sense indicators observed in this sample is not large enough to be considered reliable. Minor normal and reverse components are a function of shear zone dip and symmetry (monoclinic vs. triclinic).

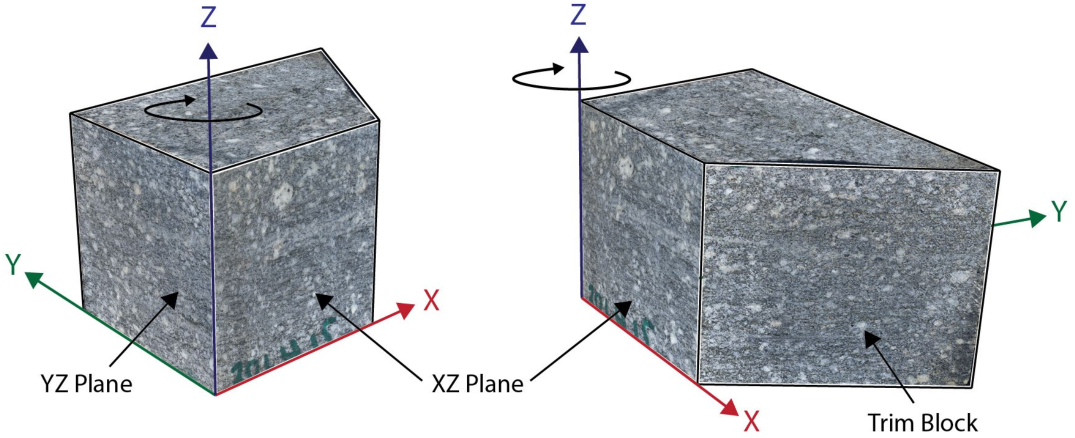

Figure 20. Example of faces observed in thin section with respect to the X, Y, and Z directions (sample 20LH15). Figure rendered using the program *Blender 2.9.2.*

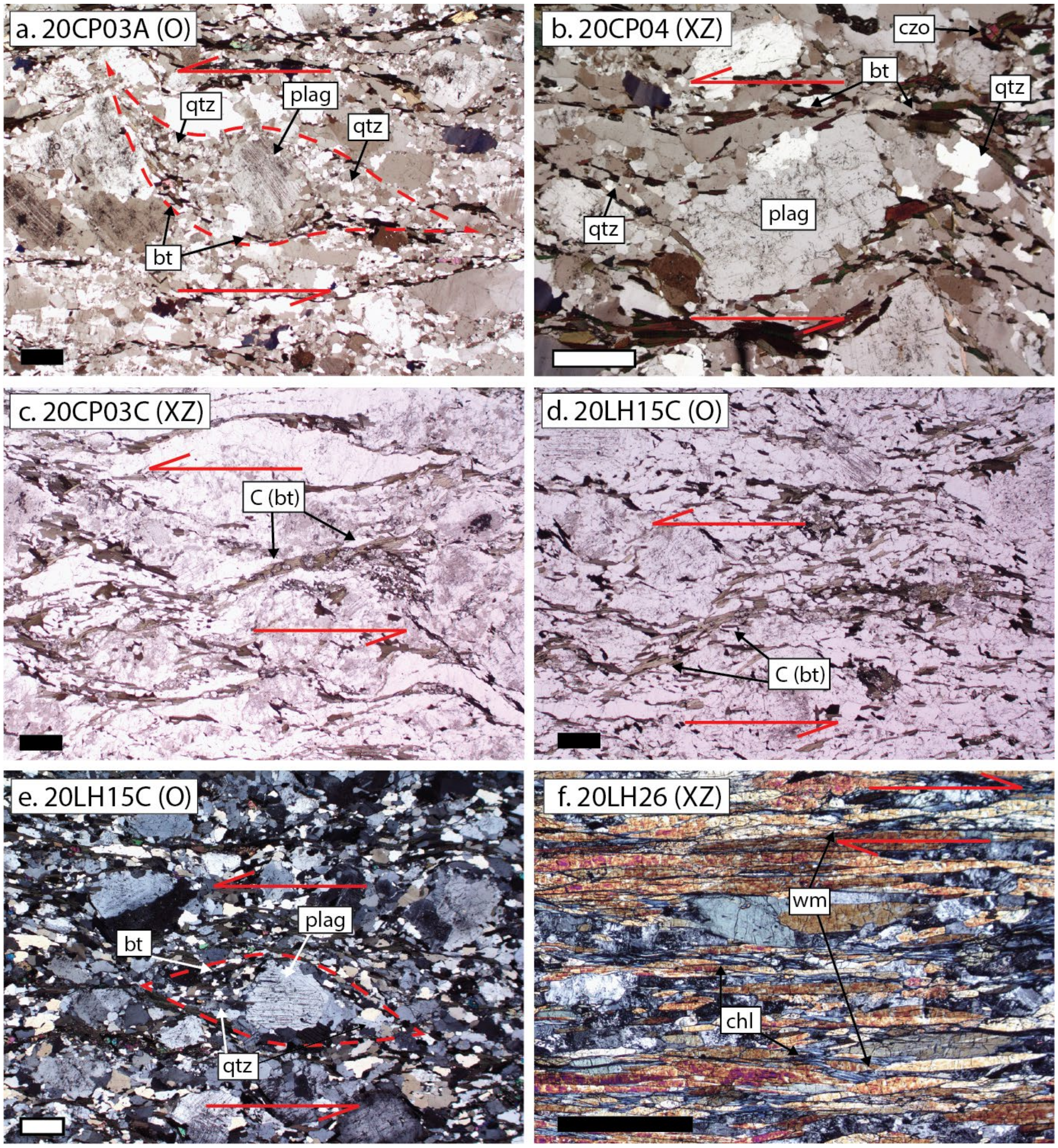

Figure 21. Microstructural evidence of sense of shear within the GSZ, the scale bar is equal to 1 mm. In all XZ samples, X is horizontal and Z is vertical with respect to the page. (a) delta clast comprised of plagioclase (plag) with quartz (qtz) and biotite (bt) pressure shadows exhibiting sinistral sense of shear, (b) backrotated delta clast comprised of plagioclase with quartz and biotite pressure shadows exhibiting sinistral sense of shear, (c & d) biotite shear bands exhibiting sinistral sense of shear, (e) sigma clast comprised of plagioclase with quartz and biotite pressure shadows exhibiting weak sinistral sense of shear, (f) white mica (wm) fish exhibiting dextral sense of shear. Scale bars are equal to 1 mm.

4.3 Anatomy and Kinematics of Cenozoic Faulting

Five named fault zones associated with late Cenozoic deformation were encountered at Lake Hauroko, Lake Monowai, Borland Road, and Mount Watson (Figures 22 & 23) . Brittle fault zones reactivated the margins of the GSZ. The deformation that produced the faults also produced a brittle overprint inside the GSZ that can be seen both in the field and in thin section. In this thesis, we use the term fault zone to include the fault core and damage zone associated with a fault. Components of fault cores include gouge, cataclasite, and mylonite, whereas damage zones contain smaller faults, fractures, veins, and folds (Caine et al., 1996). This distinction is important to consider when characterizing faults and dividing measurements into populations because the primary slip plane associated with the named faults may have been inferred using measurements from the dominant populations.

Fault populations were determined by plotting fault plane measurements on equal area lower-hemisphere stereonets in order to group faults according to the orientation of the fault plane and slickenlines. Field observations of fault characteristics such as scale, length, and offset, were used to determine which of these populations would be considered the dominant fault set. In this section, we will describe the dominant fault populations observed within the fault zones (Figures 22 & 23). In addition, we will present each dominant fault populations fault plane solution with kinematic tensors, and block diagrams associated with each major population (Figure 24). A comprehensive table of fault related data can be found in Appendix C (pg. 94).

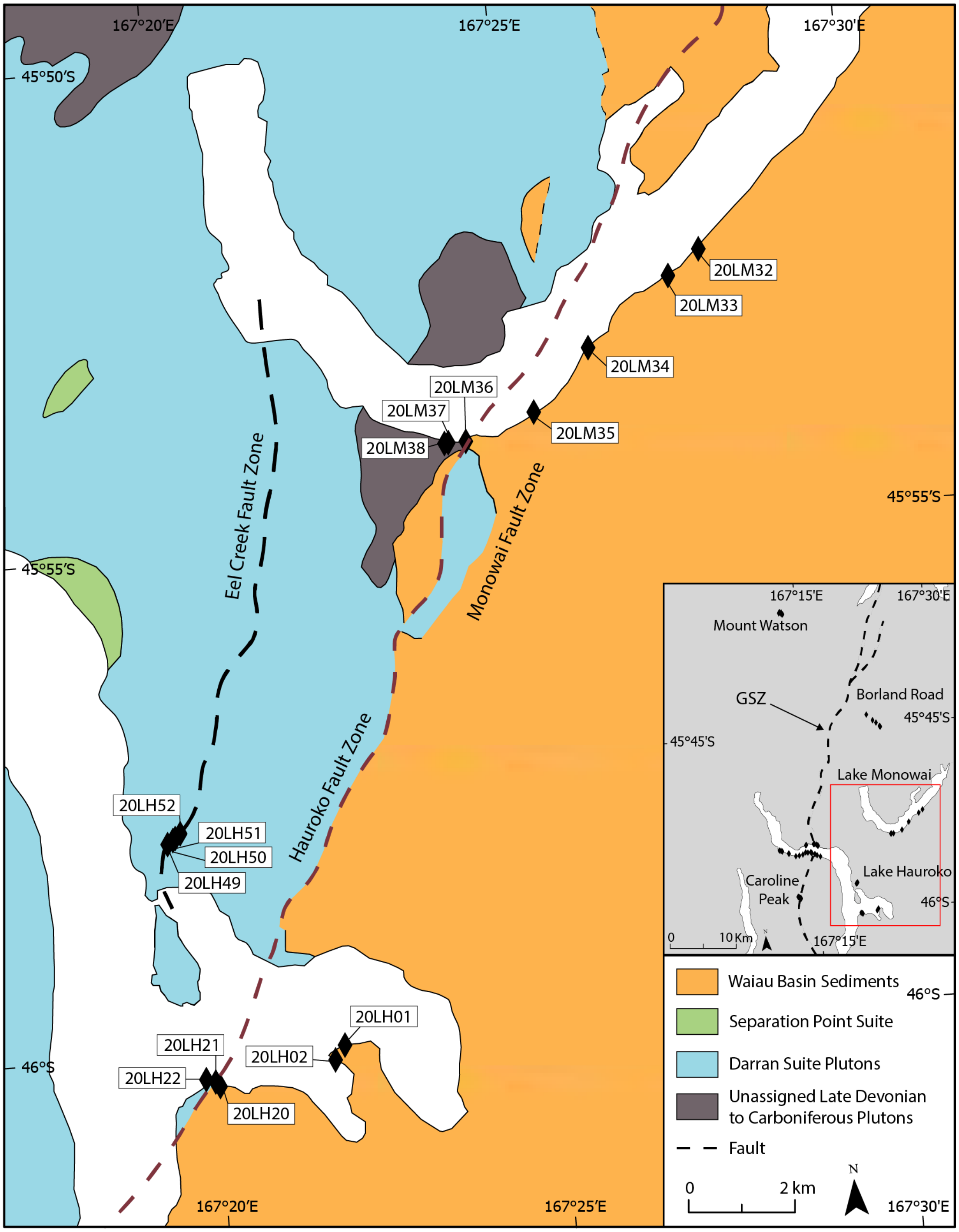

Figure 22. Locations of the Lake Hauroko, Lake Monowai, and Eel Creek fault zones within the study area.

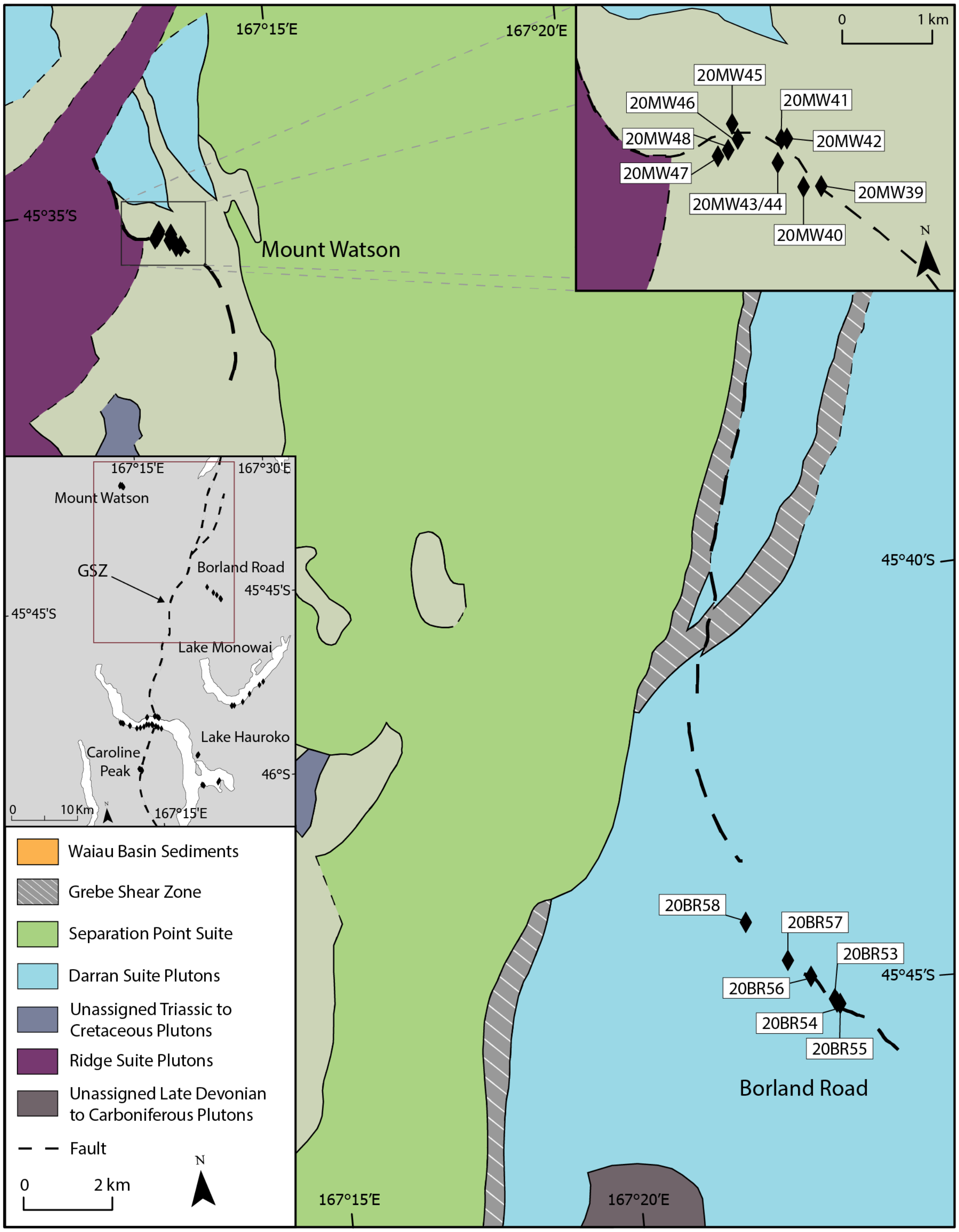

Figure 23. Locations of the Borland Road and Mount Watson fault zones within the study area.

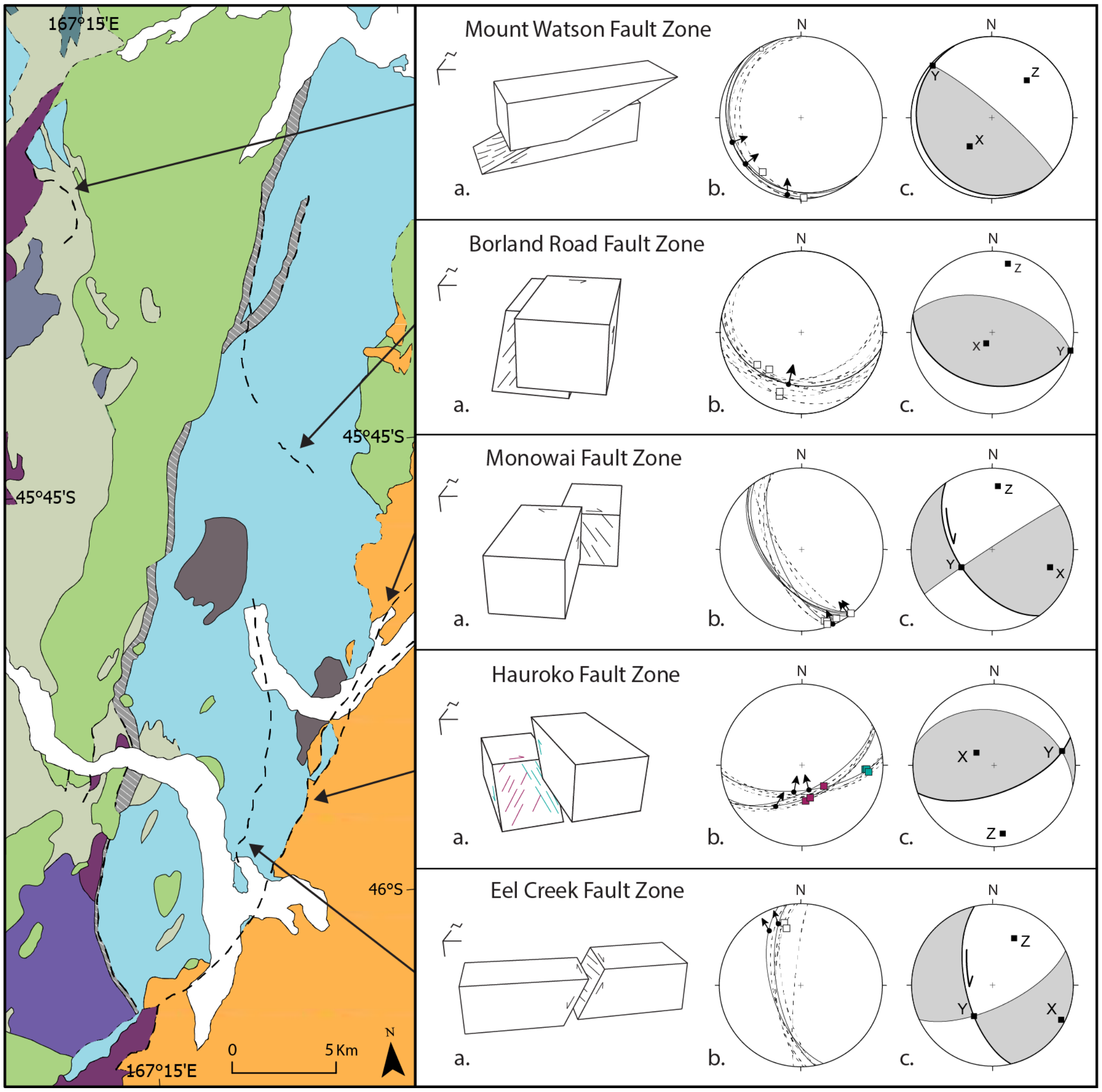

Figure 24. Block diagram (a), stereonet of fault planes and slickenlines (b) and fault plane solution (c) associated with the dominant fault populations. Solid lines on stereonet (b) correlate with solid black circles and arrows to give complete fault data used in the calculation of the fault plane solution. Dashed lines and hollow squares represent fault planes and slickenlines where the sense of slip was not obtained. Solid lines on sterenet (c) which intersect Y represent the slip surface.

	Station	**Fault Planes**		**Slickenlines**		**Slip Sense**
		Strike	Dip	Trend	Plunge	
Mount Watson Fault Zone	20MW40	**185**	**20**	**178**	**02**	**reverse**
		165	12	330	03	-
	20MW41	**180**	**14**	**190**	**04**	**reverse**
	20MW44	170	26	215	20	reverse/sinistral
		136	**12**	**250**	**06**	**reverse/sinistral**
		136	**12**	**230**	**02**	**reverse/sinistral**
Borland Road Fault Zone	20BR55	**101**	**35**	**194**	**36**	**reverse**
		119	36	234	34	-
		101	40	221	40	-
		108	29	-	-	-
		134	22	199	19	-
		109	35	200	24	-
	20BR58	073	42	-	-	-
		078	43	-	-	-
		084	23	-	-	-
		091	37	-	-	sinistral
		093	44	-	-	-
		096	31	-	-	-
		091	29	-	-	-
		098	22	-	-	-
		092	44	-	-	-
		097	42	-	-	-
		103	36	-	-	-
		084	23	-	-	-
		084	23	-	-	-
Monowai Fault Zone	20LM32	153	71	-	-	-
		144	73	330	08	-
		158	65	162	09	-
		160	**58**	**157**	**02**	**dextral**
		152	59	-	-	-
	20LM34	**140**	**52**	**142**	**02**	**dextral**
		140	**56**	**142**	**03**	**dextral**
		142	**53**	**144**	**03**	**dextral**

	Station	**Fault Planes**		**Slickenlines**		**Slip Sense**
		Strike	Dip	Trend	Plunge	
Hauroko Fault Zone	20LH21	065	75	-	-	-
		055	70	-	-	reverse
	20LM32	088	60	094	22	**reverse**
		071	52	-	-	-
		090	51	-	-	-
		078	53	-	-	-
		085	60	096	18	-
		082	58	094	21	-
	20LM34	**062**	**64**	**164**	**64**	**reverse**
		084	**64**	**194**	**92**	**reverse**
		065	**57**	**212**	**40**	**sinistral**
		063	60	166	55	**-**
		060	55	174	53	-
		058	58	083	35	-
Eel Creek Fault Zone	20LH50	**170**	**66**	**340**	**21**	**dextral**
		164	**60**	**330**	**24**	**dextral**
		185	84	-	-	**-**
		170	72	346	29	-
		176	64	345	22	-
		169	62	143	64	-
		178	65	146	63	-

Table 5. Dominant fault populations for each fault zone. Dashes indicate an absense of data. Bolded measurements were used in the calculation of the fault plane solution.

4.3.1 Reactivation of the Grebe Shear Zone

Brittle faulting was observed at the eastern edge of the GSZ at Caroline Peak, and on the western edge of the GSZ at Lake Hauroko. In both locations, the zones were localized areas of cataclastic deformation with fault surfaces at varying orientations. Complete fault-slip (including fault plane orientation, slickenline orientation, and sense of slip) was not obtained for these faults due to the varying quality of exposures along Lake Hauroko and at Caroline Peak. Therefore, these data were not visualized using fault plane solutions. Instead, sense of shear was observed at some locations, which we used to characterize fault motion. At Caroline Peak, chatter marks were observed on a brittle fault surface exhibiting west-side-up movement sense. Evidence for reactivation was also observed in thin section (Figure 24), where brittle overprint and deformation of foliations was observed in sections from samples 20LH14D, 20LH16B, and 20LH26 (Figure 10). Offset in brittle overprint and boudinaging of quartz ribbons record dextral shear sense.

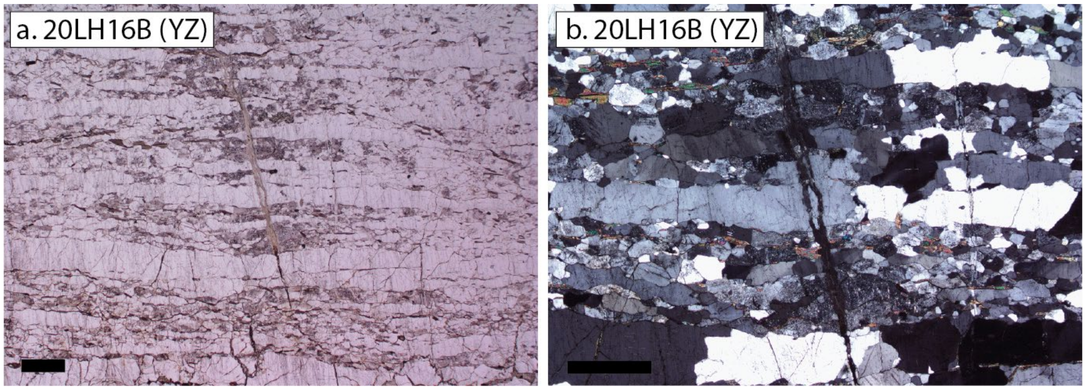

Figure 25. Microstructural evidence for reactivation in the form of a vein and brittle fractures in sample 20LH16B. Scale bars are equal to 1 mm. Y is horizontal and Z is vertical.

4.3.2 Hauroko Fault Zone

The Hauroko Fault Zone was observed at both Lake Hauroko and Lake Monowai (Figure 21). In both areas it is a zone of brittle deformation composed of multiple fault sets. At Lake Monowai, the dominant set was observed as east-northeast striking (058-090°) and moderately dipping to the south-southeast (51-64°). Slickenlines associated with this portion of the fault cluster into two groups; plunging gently (18-35°) to the east (083-096°) and plunging moderately (40-60°) to the south (134-196°) (Table 5). Field observations of chatter marks are indicative of reverse with top to the northeast sense of motion associated with south plunging slickenlines. This motion is cross-cut by the east plunging slickenlines, which had chatter marks indicative of left-lateral strike-slip motion. These observations are consistent with thrust motion followed by sinistral motion on the Hauroko fault (Figure 23). The measured faults at Lake Monowai are likely synthetic to the dominant Hauroko Fault surface due to their similar orientations. Shear fractures conjugate to the Hauroko Fault were observed at stations 20LH20 and 20LH21 and were primarily east-southeast striking (090-114°) and steeply dipping (65-81°) to the south-southeast.

4.3.3 Monowai Fault Zone

The Monowai fault zone parallels the Hauroko fault zone until its' termination at the intersection of the two zones immediately to the south of Lake Monowai (Figure 21). The Monowai fault zone presented similarly to the Hauroko fault zone in where deformation was concentrated on several sets of brittle faults. Due to the close proximity of these zones to each other and their similar deformation styles, fault measurements of each zone were taken at the same stations (20LM32 and 20LM34). The dominant fault set associated with the Monowai fault zone was observed to be southeast striking (140-160°) and moderately dipping (52-73°) to the southwest. Slickenlines on the fault plane plunge gently (02-09°) to the southeast (142-162°) (Table 5). Field observations of chatter marks record a dextral strike-slip sense of shear (Figure 23). Previously published data recorded dextral strike-slip sense along the Monowai fault with orientations consistent to those found in our study (Turnbull et al., 2010), therefore we are able to confidently delineate the fault zones in our data despite their overlap in the field.

4.3.4 Eel Creek Fault Zone

The Eel Creek fault zone was observed at Lake Hauroko (Figure 21) where it exhibits a fault surface that strikes to the south-southeast (164-185°) and dips moderately to steeply (62-84°) to the west (Table 5). Slickenlines plunge gently (21-29°) to the northwest (330-346°) on the fault plane. Chatter marks suggest right-lateral movement, which is consistent with the calculated fault plane solution exhibiting mostly strike-slip motion with a minor normal component (Figure 23). The slip direction and sense of motion on this fault has not been reported previously.

4.3.5 Borland Road Fault Zone

Fault populations were exceptionally difficult to discern at Borland Road stations because many of the outcrops were highly fractured and eroded. The dominant fault set was observed at stations 20BR55 and 20BR58 along Borland Road (Figure 22) and strikes to the east-southeast (073-139°) and dips moderately (22-44°) to the south (Table 5). Slickenlines associated with the dominant fault set plunge gently to moderately (19-40°) to the southwest (194-234°). Sense of slip was obtained from an offset pegmatite on one dominant fault surface in this fault population and records a sinistral-thrust sense of motion (Figure 23). Several minor fault sets were also observed and broadly categorized based on their orientations and scale relative to each other (Appendix C).

4.3.2 Mount Watson Fault Zone

The dominant fault set at Mount Watson (Figure 22) strikes to the south-southeast (136-185°) and dips shallowly (2-26°) to the west (Table 5). Slickenlines associated with the dominant fault set are variable, plunging gently (02-20°) to the south and northwest (170-330°). The variability in slickenline trends implies either multiple episodes of movement, or a progressive change in movement direction. Cross cutting relationships between slickenlines were not observed, therefore the order in which slip motions occurred cannot be adequately determined. Field observations of offset dikes and clasts of plagioclase with asymmetric tails of biotite record a thrust sense with a component of sinistral shear (Figure 23).

4.4 Summary of Results

In our study of the southern portion of the GSZ, we have found that the shear zone is primarily composed of an amphibolite facies assemblage of minerals that underwent retrogression to greenschist facies. This is evident by the presence of relic hornblende, the formation of clinozoisite and chlorite within foliation domains, and the formation of biotite, white mica, and chlorite in pressure shadows. Thin sections from samples surrounding the shear zone showed similar metamorphic conditions, with the common theme of retrogression to greenschist facies pressure and temperature conditions persisting at both Lake Hauroko and Caroline Peak. We have discerned a sequence of events for the shear zone and surrounding area in where the dominant fabric is protomylonitic to mylonitic in texture (S_{Grebe}) and is cross-cut by variably deformed granitic intrusions and brittle faults. Foliations within the shear zone are relatively parallel to its' boundaries, with an apparent deflection in orientations of previously existing foliations outside of the GSZ. Mineral stretching lineations vary in plunge from Caroline Peak to the north shore of Lake Hauroko, with the steepest plunging being on the south shore of Lake Hauroko.

We have found that feldspars record low strains (Figure 16), suggesting that the majority of the strain is accommodated by quartz and other matrix minerals. This is consistent on the microstructural scale, as evidence of high-strain, including grain size reduction and the dynamic recrystallization of quartz ribbons, were observed in thin section. Other examples include delta-type porphyroclasts from Caroline Peak, which suggest high strain rates (van den Driessche & Brun, 1987). Three-dimensional strain results in feldspars and quartz show a low magnitude of predominantly stretching strain. In thin section, sense of shear indicators including porphyroclasts with strain shadows, shear bands, and mineral fish record the highest degree of asymmetry on the XZ face of samples. However, asymmetric features also occur on the YZ and trim block faces of some samples. This implies that components of both pure and simple shear acted simultaneously to produce these structures. The main shear sense observed within the GSZ translates to sinistral motion in geographic coordinates, with minor normal and reverse components being a function of shear zone dip and symmetry (monoclinic vs. triclinic).

The results of fault-slip analysis show that at least one of the five fault systems underwent multiple deformational events and subsequently endured a change in both stresses and shear direction (evident by cross-cutting slickenlines). The Hauroko fault records two separate slip events during the Cenozoic: the first being reverse motion, and the second sinistral strike-slip. Two sets of slickenline orientations were also observed at Mount Watson, however cross-cutting relationships were not observed. Therefore, the change in orientation may be the result of a progressive change in stress directions. The Monowai and Eel Creek fault zones exhibit primarily dextral strike-slip motion, and the Borland Road fault zone exhibits reverse motion. Fault-slip analysis concludes that strain during the Cenozoic reactivation was partitioned across several structures.

CHAPTER 5: DISCUSSION

5.1 Characterizing Cretaceous Transpression

Initially, we hypothesized that the portion of the GSZ around Lake Hauroko and Caroline Peak would exhibit a non-partitioned, triclinic style of transpression similar to that of the northern strand (Scott et al., 2011, Buriticá et al., 2019). In order for this prediction to hold true, several conclusions must be met. First, to characterize this shear zone as transpressional, a component of shortening across the shear zone boundaries must accompany the strike-slip deformation (Dewey et al., 1998). Finite strain analysis of feldspars in and around the GSZ shows mostly oblate FSE's, which is consistent with a component of flattening across the shear zone. This result is supported by the near parallel to the shear zone boundary orientation of axial planes of isoclinal folds in rocks to the east of the shear zone (station 20LH31), which suggests shortening across the shear zone. In addition, because both the strike-slip and shortening components were accommodated together on the same structures within the same narrow zone, the deformation can be characterized as a non-partitioned style of transpression.

The symmetry of this transpressional system was inferred using the results of our kinematic analysis. In general, the highest degree of asymmetry within shear zones samples were along the XZ plane, suggesting that some portions of the system exhibit approximately monoclinic symmetry. However, in some samples (20LH14C & 20LH15) (Table 3) the planes of maximum asymmetry were observed at angles to the XZ plane, which is indicative of triclinic symmetry (Díaz-Azpiroz et al., 2014). Therefore, the shear zone can be described as primarily monoclinic with some weak evidence of triclinic symmetry. These results establish that the geometry of deformation, including the shear plane and the shear direction within a few segments of the GSZ, must be characterized in three dimensions (triclinic) rather than two (monoclinic). This result is interesting because it shows that not all segments of the shear zone exhibit similar shear geometries. It also is important for assessing the regional significance and magnitude of motion accommodated by the structure.

5.1.1 Comparison with Previous Results

The portion of the GMZ near Lake Manapouri has previously been described as an amphibolite facies shear zone that accommodated sinistral-reverse (Scott et al., 2011) and sinistral motion (Buriticá et al., 2019). In addition, Buriticá et al. (2019) concluded that the western boundary of the shear zone near Lake Manapouri exhibits an apparent normal-sense motion and predicted that thrust-sense motion may also occur on the eastern boundary, which is a consequence of inclined transpression (Jones et al., 2004). We speculate that this style of motion may reflect the reactivation of an ancient, dipping fault zone that formed during Paleozoic times and later, during the Cretaceous, became the GSZ (Klepeis et al., 2019). Further to the south near Lake Hauroko, we have found that Cretaceous transpression accommodated a combination of sinistral-slip and reverse-slip motion in single, a narrow zone (~1 km) of ductile deformation. The results of our kinematic analysis suggest that the geometry of transpressional deformation was close to monoclinic near Caroline Peak but shows some triclinic symmetry near Lake Hauroko.

These results are consistent with mineral stretching lineations observed in the field, which plunge more steeply at Lake Hauroko than at Caroline Peak. The dominantly monoclinic symmetry suggests that simple shear dominated over pure shear during deformation, however evidence of pure shear dominated transpression was also observed at Lake Hauroko. This is also consistent with the results of McGinn et al. (2020) who, using electron backscatter diffraction (EBSD), concluded that simple shear dominated over pure shear during the initiation of transpression.

Buriticá et. al (2019) defined both early low-strain and later high-strain fabrics in the GSZ near Lake Te Anau (Figure 26). They described high-strain fabrics in granitic gneisses that contain moderately to steeply dipping foliations and moderate- to steeply-plunging mineral stretching lineations. This geometry is similar to the shear zone fabrics we observed much farther south near Lake Hauroko. However, we were unable to discern more than one episode of shearing with the southern segment of the GSZ. This contrasts with the results of Buriticá et al. (2019) who found at least two distinctive episodes of deformation produced low-strain zones at 129-125 Ma and high-strain zones at 125-116 Ma.

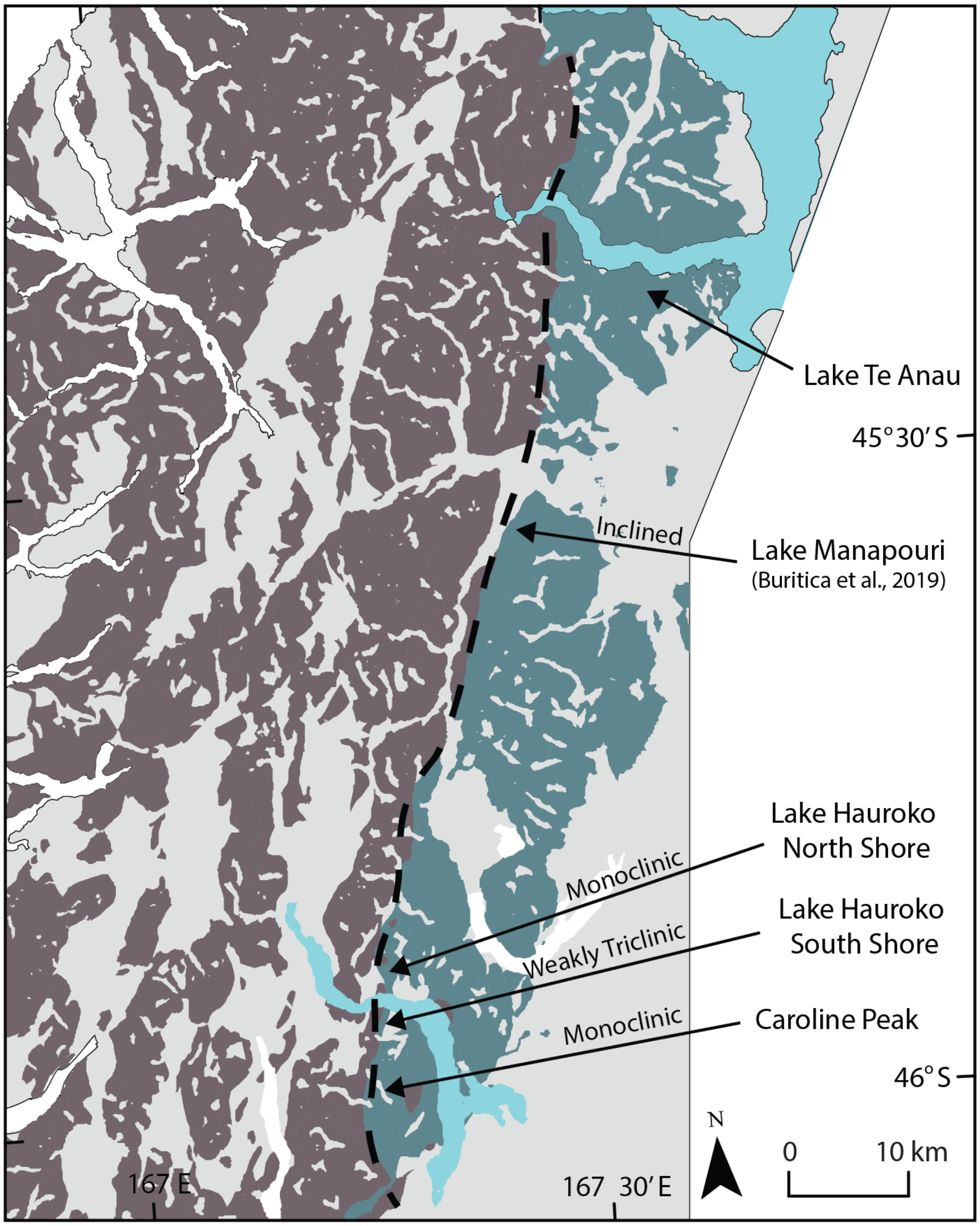

Figure 26. The GSZ at Caroline Peak, Lake Hauroko, Lake Monowai, and Lake Te Anau and its associated geometries.

5.2. Characterizing Cenozoic Transpression

Later Cenozoic faulting also is interpreted to be transpressional in nature. The results of instantaneous strain and kinematic analysis show that three of the five fault systems we examined exhibited primarily reverse dip-slip motion, with the remaining two exhibiting strike slip motion (Figure 24). In this case, the transpression is partitioned into separate structures that accommodate the strike-slip and reverse components of oblique convergence, respectively. Strain partitioning has been shown to preferentially occur in situations where pre-existing zones of weakness such as faults, shear zones, and lithologic boundaries influence the geometry of deformation (Jones & Tanner, 1995). The former transpressional deformation event created a structural anisotropy in where strike-slip motion could be accommodated separate from reverse motion, which appears common in zones of reactivation.

5.2.1 Tectonic Implications

A study previously conducted by Klepeis et. al (2019) involving $^{40}Ar/^{39}Ar$ geochronology concluded that five episodes of reactivation on fault zones that parallel the Puysegur Trench occurred in the Miocene-Pliocene (Figure 1). Our study area captures at least two of the most recent of these faulting events. Using conjugate shear fractures at the Hauroko fault, we can infer that the axis of maximum principal compression (σ_1) was oriented approximately 085°. This fault is denoted as active and continues to the south offshore of the South Island, where the present plate movement vector between the Australian and Pacific plates is oriented at approximately 060°.

Though most of the present-day expression of the collision between the Australia and Pacific plates occurs at the Alpine Fault (Turnbull et al., 2010), our fault orientation data suggest that some of this movement may have been accommodated by faults located at least 100 km inland from the plate boundary, including the Hauroko fault near Lake Hauroko. This result illustrates that oblique plate convergence near Fiordland is both partitioned and distributed across a wide zone in SW New Zealand.

5.3 Future Work

The aforementioned result implies that structures associated with present day plate movement have the potential to form in areas other than the Alpine Fault Zone, which may warrant future work on the relationship between ancient structures and present-day active faulting. Additionally, a more comprehensive study on strain in quartz with respect to feldspar would provide valuable insight into the role that strain plays in middle to upper crustal shear zone deformation. These results can be compared with those of middle to lower crustal shear zones within Fiordland to provide a comprehensive understanding of how shear zones behave at different crustal depths.

CHAPTER 6: CONCLUSIONS

The results of this study show that there are two different types of superposed transpressional deformation that have different origins and occurred at different times within southern Fiordland. Cretaceous transpression produced the Grebe shear zone, which is a non-partitioned transpressional system in where sinistral strike-slip motion and shortening are accommodated in the same narrow (~1 km wide) zone of deformation. The deformational symmetry of the GSZ is close to monoclinic near Caroline Peak and triclinic near Lake Hauroko. Previous studies conducted on the northern section of the GSZ by Buriticá et. al (2019) concluded that the shear zone exhibits inclined transpressional deformation. Our results are compatible with these results, although they also show that the geometry of deformation is variable along its length. In some places, such as Caroline Peak, the deformation is characterized by sinistral-normal (west-side-down) motion in a zone displaying approximately monoclinic symmetry. In others, such as Lake Hauroko, the deformation exhibits sinistral shear with a component of west-side-down apparent reverse motion. This suggests that the GSZ is highly variable both along and across strike to the scale of tens of kilometers. Reactivation of the Cretaceous shear zone defines the second transpressional style in where the shortening and strike-slip components are accommodated in different structures, primarily across brittle faults. This study allowed us to observe the influence of a previously existing shear zone on later deformation, and more specifically, strain partitioning. The GSZ represents a weakness in the rock of an ancient plate boundary, which was able to preferentially accommodate strain during reactivation.

Several methods were used in concert to one another in order to characterize our portion of the GSZ. The results of our study could be severely compromised if we removed any one of these methods. For example, if we attempted to discern the transpressional symmetry without kinematic analysis, we would introduce a large component of error due to the reliability of our strain results. Therefore, this study subsequently emphasizes the importance of characterizing the shear zone in three-dimensions and using multiple methods of analysis to corroborate our results.

BIBLIOGRAPHY

Allmendinger, R.W., Cardozo, N., and Fisher, D.M., 2012, Structural geology algorithms: vectors and tensors: Cambridge ; New York, Cambridge University Press, 289 p.

Buriticá, L.F., Schwartz, J.J., Klepeis, K.A., Miranda, E.A., Tulloch, A.J., Coble, M.A., and Kylander-Clark, A.R.C., 2019, Temporal and spatial variations in magmatism and transpression in a Cretaceous arc, Median Batholith, Fiordland, New Zealand: Lithosphere, v. 11, p. 652–682, doi:10.1130/L1073.1.

Caine, J.S., Evans, J.P., and Forster, C.B., 1996, Fault zone architecture and permeability structure: Geology, v. 24, p. 1025-1028, doi: 10.1130/0091-7613(1996)024<1025:FZAAPS>2.3.CO;2.

Cardozo, N., and Allmendinger, R.W., 2013, Spherical projections with OSXStereonet: Computers & Geosciences, v. 51, p. 193–205, doi:10.1016/j.cageo.2012.07.021.

Dewey, J.F., Holdsworth, R.E., and Strachan, R.A., 1998, Transpression and transtension zones: Geological Society, London, Special Publications, v. 135, p. 1–14, doi:10.1144/GSL.SP.1998.135.01.01.

Díaz-Azpiroz, M., Barcos, L., Balanyá, J.C., Fernández, C., Expósito, I., and Czeck, D.M., 2014, Applying a general triclinic transpression model to highly partitioned brittle-ductile shear zones: A case study from the Torcal de Antequera massif, external Betics, southern Spain: Journal of Structural Geology, v. 68, p. 316–336, doi:10.1016/j.jsg.2014.05.010.

Díaz-Azpiroz, M., Fernández, C., and Czeck, D.M., 2019, Are we studying deformed rocks in the right sections? Best practices in the kinematic analysis of 3D deformation zones: Journal of Structural Geology, v. 125, p. 218–225, doi:10.1016/j.jsg.2018.03.005.

Druguet, E., Alsop, G.I., and Carreras, J., 2009, Coeval brittle and ductile structures associated with extreme deformation partitioning in a multilayer sequence: Journal of Structural Geology, v. 31, p. 498–511, doi:10.1016/j.jsg.2009.03.004.

Ducea, M.N., Saleeby, J.B., and Bergantz, G., 2015, The Architecture, Chemistry, and Evolution of Continental Magmatic Arcs: Annual Review of Earth and Planetary Sciences, v. 43, p. 299-331, doi 10.1146/annurev-earth-060614-105049.

Fisher, N. I., Lewis, T., and Embleton, B. J., 1993, Statistical analysis of spherical data, Cambridge university press. Sciences, v. 43, p. 299–331, doi:10.1146/annurev-earth-060614-105049.

Fossen, H., 2010, Structural Geology. Cambridge University Press, Cambridge, 463 p.

Fossen, H., and Cavalcante, G.C.G., 2017, Shear zones – A review: Earth-Science Reviews, v. 171, p. 434–455, doi:10.1016/j.earscirev.2017.05.002.

Fossen, H., and Tikoff, B., 1993, Deformation matrix for simultaneous simple shearing, pure shearing and volume change, and its application to transpression-transtension tectonics: Journal of Structural Geology, v. 15, p. 413-422, doi:10.1016/0191-8141(93)90137-Y.

Fossen, H., Tikoff, B., and Teyssier, C.T., 1994, Strain modeling of transpressional and transtensional deformation: Norsk Geologisk Tidsskrift, v. 74, p. 134-145.

Goodwin, L.B., and Tikoff, B., 2002, Competency contrast, kinematics, and the development of foliations and lineations in the crust: Journal of Structural Geology, v. 24, p. 1065–1085, doi:10.1016/S0191-8141(01)00092-X.

Hartland, W.B., 1971, Tectonic transpression in Caledonian Spitsbergen: Geological Magazine, v. 108, p. 27–41, doi:10.1017/S0016756800050937.

Hossack, J.R., 1968, Pebble deformation and thrusting in the Bygdin area (Southern Norway): Tectonophysics, v. 5, p. 315–339, doi:10.1016/0040-1951(68)90035-8.

Jiao, R., Herman, F., and Seward, D., 2017, Late Cenozoic exhumation model of New Zealand: Impacts from tectonics and climate: Earth-Science Reviews, v. 166, p. 286–298, doi:10.1016/j.earscirev.2017.01.003.

Jones, R.R., Holdsworth, R.E., Clegg, P., McCaffrey, K., and Tavarnelli, E., 2004, Inclined transpression: Journal of Structural Geology, v. 26, p. 1531–1548, doi:10.1016/j.jsg.2004.01.004.

Jones, R.R., Holdsworth, R.E., McCaffrey, K.J.W., Clegg, P., and Tavarnelli, E., 2005, Scale dependence, strain compatibility and heterogeneity of three-dimensional deformation during mountain building: a discussion: Journal of Structural Geology, v. 27, p. 1190–1204, doi:10.1016/j.jsg.2005.04.001.

Jones, R.R., and Tanner, G.P.W., 1995, Strain partitioning in transpression zones: Journal of Structural Geology, v. 17, p. 783–802, doi:10.1016/0191-8141(94)00102-6.

Kamb, W. B., 1959, Ice petrofabric observations from Blue Glacier, Washington, in relation to theory and experiment: Journal of Geophysical Research., v. 64, p. 1891– 1909, doi:10.1029/JZ064i011p01891.

Klepeis, K.A., Webb, L.E., Blatchford, H.J., Jongens, R., Turnbull, R.E., and Schwartz, J.J., 2019a, The Age and Origin of Miocene-Pliocene Fault Reactivations in the Upper Plate of an Incipient Subduction Zone, Puysegur Margin, New Zealand: Tectonics, v. 38, p. 3237–3260, doi:10.1029/2019TC005674.

Klepeis, K., Webb, L., Blatchford, H., Schwartz, J., Jongens, R., Turnbull, R., and Stowell, H., 2019b, Deep Slab Collision during Miocene Subduction Causes Uplift along Crustal-Scale Reverse Faults in Fiordland, New Zealand: GSA Today, v. 29, p. 4–10, doi:10.1130/GSATG399A.1.

N. H. W., 1986, R. J. Lisle 1985. Geological Strain Analysis: A Manual for the Rf/φ Technique: Geological Magazine, v. 123, p. 323–323, doi: 10.1017/S0016756800034920.

Luyendyk, B.P., 1995, Hypothesis for Cretaceous rifting of east Gondwana caused by subducted slab capture: Geology, v. 23, p. 373-376, doi:10.1130/0091-7613

Marcotte, S.B., Klepeis, K.A., Clarke, G.L., Gehrels, G., and Hollis, J.A., 2005, Intra-arc transpression in the lower crust and its relationship to magmatism in a Mesozoic magmatic arc: Tectonophysics, v. 407, p. 135–163, doi:10.1016/j.tecto.2005.07.007.

Marrett, R., and Allmendinger, R.W., 1990, Kinematic analysis of fault-slip data: Journal of Structural Geology, v. 12, p. 973–986, doi:10.1016/0191-8141(90)90093-E.

McGinn, C., Miranda, E.A., and Hufford, L.J., 2020, The effects of quartz Dauphine twinning on strain localization in a mid-crustal shear zone: Journal of Structural Geology, v. 134, doi: 10.1016/j.jsg.2020.103980.

Means et al., 1980, Vorticity and non-coaxiality in progressive deformations: Journal of Structural Geology, v. 2, p. 371-378, doi: 10.1016/0191-8141(80)90024-3.

Mortimer, N., 2004, New Zealand's Geological Foundations: Gondwana Research, v. 7, p. 261–272, doi:10.1016/S1342-937X(05)70324-5.

Mortimer, N. et al., 2017, Zealandia: Earth's Hidden Continent: GSA Today, v. 27, p. 27–35, doi:10.1130/GSATG321A.1.

Mortimer, N., Tulloch, A.J., Spark, R.N., Walker, N.W., Ladley, E., Allibone, A., and Kimbrough, D.L., 1999, Overview of the Median Batholith, New Zealand: a new interpretation of the geology of the Median Tectonic Zone and adjacent rocks: Journal of African Earth Sciences, v. 29, p. 257–268, doi:10.1016/S0899-5362(99)00095-0.

Passchier, C. W. and Trouw, R. A., 2005, Microtectonics, Springer Science & Business Media, 366 p.

Robin, P.-Y.F., 2002, Determination of fabric and strain ellipsoids from measured sectional ellipses - theory: Journal of Structural Geology, v. 24, p. 531-544, doi: 10.1016/S0191-8141(01)00081-5 .

Sanderson, D. and Marchini, W.R.D., 1984, Transpression: Journal of Structural Geology, v. 6, p. 449-458, doi:10.1016/0191-8141(84)90058-0.

Schwartz, J.J., Klepeis, K.A., Sadorski, J.F., Stowell, H.H., Tulloch, A.J., and Coble, M.A., 2017, The tempo of continental arc construction in the Mesozoic Median Batholith, Fiordland, New Zealand: Lithosphere, v. 9, p. 343–365, doi:10.1130/L610.1.

Scott, J., 2013, A review of the location and significance of the boundary between the Western Province and Eastern Province, New Zealand: New Zealand Journal of Geology and Geophysics, v. 56, p. 276–293, doi:10.1080/00288306.2013.812971.

Scott, J.M., Cooper, A.F., Tulloch, A.J., and Spell, T.L., 2011, Crustal thickening of the Early Cretaceous paleo-Pacific Gondwana margin: Gondwana Research, v. 20, p. 380–394, doi:10.1016/j.gr.2010.10.008.

Shan, Y., 2008, An analytical approach for determining strain ellipsoids from measurements on planar surfaces: Journal of Structural Geology, v. 30, p. 539–546, doi:10.1016/j.jsg.2006.12.004.

Shimamoto, T. and Ikeda, Y., 1976, A simple algebraic method for strain estimation from deformed ellipsoidal objects. 1. Basic theory: Tectonophysics, v. 36, p. 315–337, doi:10.1016/0040-1951(76)90107-4.

Teyssier, C., Tikoff, B., and Markley, M., 1995, Oblique plate motion and continental tectonics: Geology, v. 23, p. 447-450, doi: 10.1130/0091-7613(1995)023<0447:OPMACT>2.3.CO;2.

Tikoff, B. and Fossen, H., 1993., Simultaneous pure and simple shear: the unifying deformation matrix: Tectonophysics, v. 217, p. 267-283.

Turnbull, I., Allibone, A., and Jongens, R., 2010, Geology of the Fiordland Area. Institute of Geological & Nuclear Sciences 1: 250,000 Geological Map 17: Lower Hutt, GNS Science, v. 1.

Van den Driessche, J, and Brun, J.P., 1987, Rolling structures at large shear strain: Journal of Structural Geology, v. 9, p. 691-706, doi: 10.1016/0191-8141(87)90153-2.

Vauchez, A., Tommasi, A., and Mainprice, D., 2012, Faults (shear zones) in Earth's mantle: Tectonophysics, v. 558-559, p. 1-27, doi: 10.1016/j.tecto.2012.06.006.

Vollmer, F.W., 2010, A comparison of ellipse-fitting techniques for two and three-dimensional strain analysis, and their implementation in an integrated computer program designed for field-based studies. Abstract T21B-2166, Fall Meeting, American Geophysical Union, San Francisco, California.

Vollmer, F.W., 2018, Automatic contouring of geologic fabric and finite strain data on the unit hyperboloid: Computers & Geosciences, v. 115, p. 134–142, doi:10.1016/j.cageo.2018.03.006.

APPENDIX A: SUPPLEMENTAL CROSS-SECTIONS

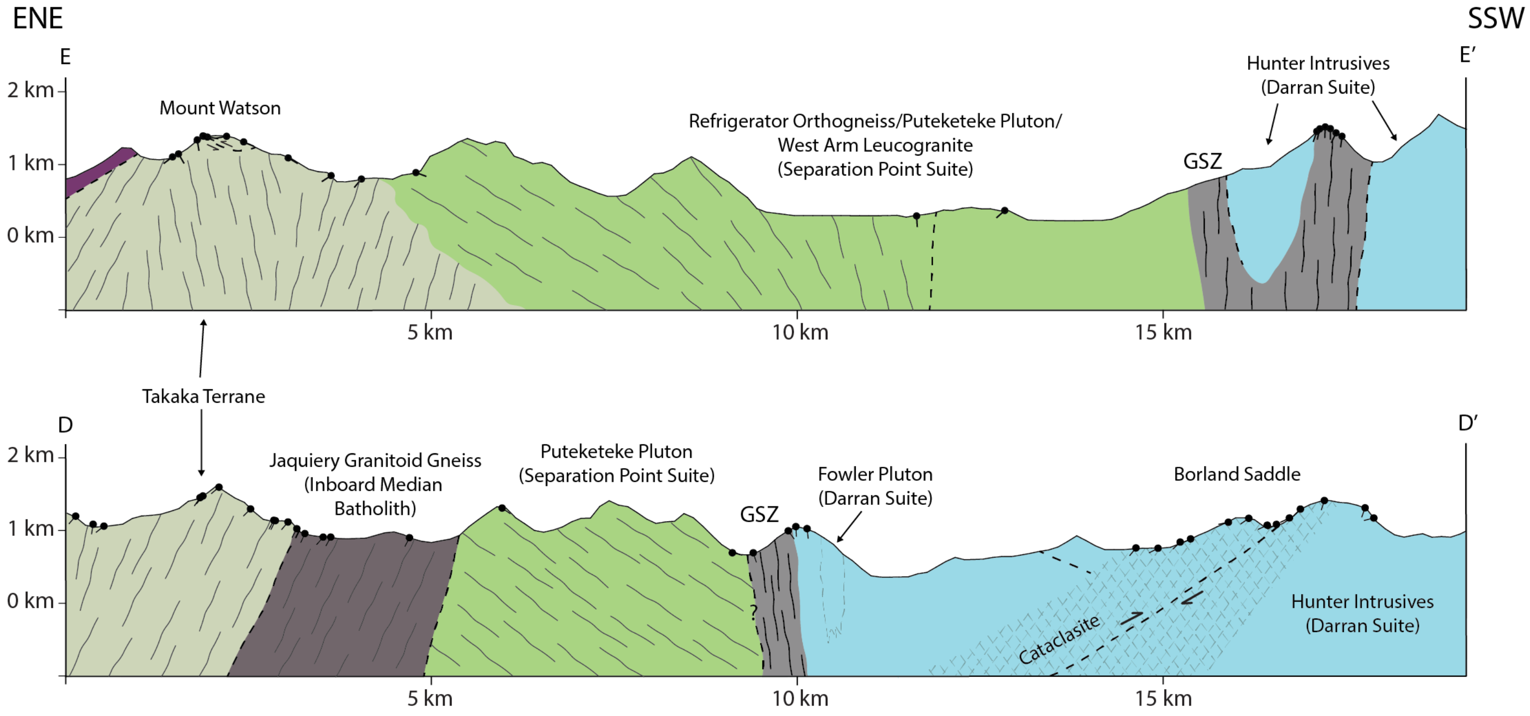

Appendix A. Cross-sections depicting subsurface geology of transects D-D’ (Borland Road) and E-E’ (Mount Watson). Ball and tick symbols represent planar measurements used to create the cross-sections. Cross-section locations and lithology key can be found in Figure 5.

APPENDIX B: COMPREHENSIVE STRAIN DATA IN FELDSPARS

20CP01

Two-Dimensional Best-Fit Ellipses

	Orientation*	**N**	**R**		**ϕ**	
20CP01_1	256 75	60	1.5019	0.1268	82.766°	6.012°
20CP01_2	344 85	60	1.3416	0.1232	173.938°	7.412°
20CP01_3	253 80	60	1.6240	0.1061	82.138°	4.845°
20CP01_4	348 85	60	1.2260	0.1268	170.843°	14.005°
20CP01_5	073 12	60	1.9623	0.1323	83.259°	3.208°

*Orientation given as strike and dip.

N = Number of Ellipses Selected

▨ = 95% Confidence Intervals

Three-Dimensional Best-Fit Ellipsoids

		Robin		**Shan**	
Max. (A)	**Length (Å)**	1.377	0.057	1.379	0.059
	Trend	155.45°	3.27°	155.44°	3.28°
	Plunge	0.36°	7.03°	0.44°	7.24°
	α		7.63°		7.83°
Int. (B)	**Length (Å)**	1.061	0.033	1.062	0.033
	Trend	249.47°	63.76°	250.32°	63.36°
	Plunge	84.83°	4.72°	84.40°	4.88°
	α		7.80°		7.97°
Min. (C)	**Length (Å)**	0.684	0.022	0.683	0.023
	Trend	65.42°	3.05°	65.40°	3.06°
	Plunge	5.16°	3.69°	5.18°	3.69°
	α		4.28°		4.25°

α = Angular Error

▨ = 95% Confidence Intervals

20CP03C

Two-Dimensional Best-Fit Ellipses

	Orientation*	N	R		ϕ	
20CP03C_1	087 47	60	1.7205	0.1360	97.106°	4.061°
20CP03C_2	005 81	60	1.1750	0.1100	135.853°	18.042°
20CP03C_3	091 31	60	1.8505	0.1220	99.738°	3.474°
20CP03C_4	289 46	60	1.7788	0.1276	78.500°	3.493°
20CP03C_5	276 42	60	1.8089	0.1375	85.190°	3.610°

*Orientation given as strike and dip.

N = Number of Ellipses Selected

▨ = 95% Confidence Intervals

Three-Dimensional Best-Fit Ellipsoids

		Robin		Shan	
Max. (A)	**Length (Å)**	1.294	0.057	1.278	0.057
	Trend	145.95°	19.92°	147.56°	24.80°
	Plunge	58.44°	18.44°	55.06°	22.11°
	α		21.04°		26.30°
Int. (B)	**Length (Å)**	1.163	0.043	1.178	0.042
	Trend	349.51°	6.92°	350.35°	8.72
	Plunge	29.38°	19.84°	32.78°	23.99
	α		20.94°		26.28
Min. (C)	**Length (Å)**	0.665	0.018	0.664	0.018
	Trend	253.52°	3.14°	253.52°	3.34
	Plunge	10.50°	2.38°	10.75°	2.34
	α		3.44°		3.56

α = Angular Error

▨ = 95% Confidence Intervals

20LH11A

Two-Dimensional Best-Fit Ellipses

	Orientation*	N	R		φ	
20LH11A_1	274 89	30	1.3255	0.1868	170.062°	12.677°
20LH11A_2	201 07	30	1.1459	0.1470	81.906°	34.808°
20LH11A_3	003 84	30	1.1261	0.1372	6.400°	37.399°

*Orientation given as strike and dip.

N = Number of Ellipses Selected

▨ = 95% Confidence Intervals

Three-Dimensional Best-Fit Ellipsoids

		Robin		Shan	
Max. (A)	**Length (Å)**	1.161	0.084	1.161	0.087
	Trend	100.70°	24.70°	100.81°	25.54°
	Plunge	9.25°	9.18°	9.14°	9.31°
	α		25.87°		26.73°
Int. (B)	**Length (Å)**	0.991	0.056	0.992	0.057
	Trend	9.23°	26.18°	9.34	26.62
	Plunge	8.95°	23.00°	9.04	23.01
	α		33.38°		34.12
Min. (C)	**Length (Å)**	0.869	0.054	0.869	0.055
	Trend	235.91°	77.61°	235.41°	77.04°
	Plunge	77.07°	21.19°	77.09°	21.44°
	α		27.85°		28.47°

α = Angular Error

▨ = 95% Confidence Intervals

20LH14A

Two-Dimensional Best-Fit Ellipses

	Orientation*	**N**	**R**		**ϕ**	
20LH14A_1	287 77	60	1.7077	0.0951	92.230°	4.044°
20LH14A_3	284 74	60	1.6183	0.1246	90.522°	5.544°
20LH14A_4	026 14	60	1.4664	0.1060	151.841°	5.568°
20LH14A_5	091 58	60	1.7894	0.1115	81.762°	4.000°
20LH14A_6	063 12	60	1.7514	0.1131	144.346°	4.262°

*Orientation given as strike and dip.

N = Number of Ellipses Selected

▨ = 95% Confidence Intervals

Three-Dimensional Best-Fit Ellipsoids

		Robin		**Shan**	
Max. (A)	**Length (Å)**	1.253	0.059	1.282	0.072
	Trend	175.14°	49.88°	180.49°	34.77°
	Plunge	72.14°	11.79°	68.48°	13.32°
	α		17.22°		16.73°
Int. (B)	**Length (Å)**	1.078	0.053	1.079	0.063
	Trend	15.11°	4.68°	17.94°	5.11°
	Plunge	16.85°	13.99°	20.61°	14.93°
	α		17.24°		16.87°
Min. (C)	**Length (Å)**	0.740	0.017	0.723	0.016
	Trend	283.36°	3.55°	285.71°	4.04°
	Plunge	5.75°	2.92°	5.91°	2.92°
	α		4.11°		4.44°

α = Angular Error

▨ = 95% Confidence Intervals

20LH14C

Two-Dimensional Best-Fit Ellipses

	Orientation*	N	R		φ	
20LH14C_1	145 74	60	1.8749	0.0959	91.474°	2.973°
20LH14C_2	236 88	60	1.4707	0.0816	49.041°	5.449°
20LH14C_3	354 16	60	1.4361	0.1071	109.863°	6.131°

*Orientation given as strike and dip.

N = Number of Ellipses Selected

▨ = 95% Confidence Intervals

Three-Dimensional Best-Fit Ellipsoids

		Robin		Shan	
Max. (A)	Length (Å)	1.413	0.059	1.470	0.069
	Trend	255.25°	6.06°	254.47°	6.07°
	Plunge	47.71°	6.08°	47.03°	6.11°
	α		6.91°		6.93°
Int. (B)	Length (Å)	0.999	0.039	0.983	0.042
	Trend	111.48°	7.16°	110.86°	7.43°
	Plunge	36.27°	6.46°	36.87°	6.49°
	α		7.58°		7.72°
Min. (C)	Length (Å)	0.708	0.026	0.692	0.026
	Trend	7.09°	5.09°	6.00°	5.32°
	Plunge	18.70°	3.46°	18.87°	3.65°
	α		5.59°		5.80°

α = Angular Error

▨ = 95% Confidence Intervals

20LH14D

Two-Dimensional Best-Fit Ellipses

	Orientation*	N	R		ϕ	
20LH14D_1	113 71	60	1.5655	0.1018	58.230°	4.198°
20LH14D_2	234 42	30	1.3770	0.1673	127.536°	9.034°
20LH14D_3	273 81	60	1.5003	0.0980	48.598°	4.704°
20LH14D_4	168 39	60	1.5054	0.1122	22.135°	5.627°
20LH14D_5	268 74	30	1.5301	0.1548	110.752°	6.238°
20LH14D_6	008 56	30	1.2035	0.1105	71.242°	16.457°
20LH14D_7	015 54	30	1.1487	0.1250	98.350°	26.654°

*Orientation given as strike and dip.

N = Number of Ellipses Selected

▨ = 95% Confidence Intervals

Three-Dimensional Best-Fit Ellipsoids

		Robin		Shan	
Max. (A)	**Length (Å)**	1.120	0.033	1.112	0.040
	Trend	104.69°	66.87°	131.40°	77.96°
	Plunge	74.08°	14.73°	65.10°	45.59°
	α		27.39°		65.47°
Int. (B)	**Length (Å)**	1.041	0.034	1.062	0.041
	Trend	1.33°	11.02°	5.90°	40.08°
	Plunge	3.77°	21.92°	15.09°	46.78°
	α		27.42°		65.49°
Min. (C)	**Length (Å)**	0.857	0.019	0.847	0.021
	Trend	270.29°	8.23°	270.47°	8.71°
	Plunge	15.44°	4.21°	19.33°	4.73°
	α		8.25°		8.60°

α = Angular Error

▨ = 95% Confidence Intervals

20LH15

Two-Dimensional Best-Fit Ellipses

	Orientation*	N	R		ϕ	
20LH15_1	250 61	60	1.5338	0.1008	105.638°	4.804°
20LH15_2	094 34	60	1.4797	0.0853	57.852°	4.611°
20LH15_3	081 89	60	1.4338	0.0972	113.649°	5.262°
20LH15_4	354 78	60	1.1776	0.0982	53.783°	17.754°
20LH15_5	097 33	60	1.3559	0.1002	61.063°	6.658°

*Orientation given as strike and dip.

N = Number of Ellipses Selected

░ = 95% Confidence Intervals

Three-Dimensional Best-Fit Ellipsoids

		Robin		Shan	
Max. (A)	**Length (Å)**	1.225	0.065	1.246	0.070
	Trend	339.28°	4.67°	337.15°	4.91°
	Plunge	35.26°	11.71°	37.42°	10.01°
	α		11.88°		10.20°
Int. (B)	**Length (Å)**	1.020	0.039	1.016	0.040
	Trend	152.58°	8.03°	154.51°	7.41°
	Plunge	54.56°	11.69°	52.55°	10.01°
	α		11.95°		10.26°
Min. (C)	**Length (Å)**	0.800	0.022°	0.790	0.024
	Trend	247.04°	4.34°	246.17°	4.27°
	Plunge	3.17°	3.21°	1.27°	3.37°
	α		5.19°		5.21°

α = Angular Error

░ = 95% Confidence Intervals

20LH23

Two-Dimensional Best-Fit Ellipses

	Orientation*	N	R		φ	
20LH23_1	255 75	30	1.8390	0.1547	60.474°	4.542°
20LH23_2	158 63	30	1.3691	0.1666	99.143°	11.584°
20LH23_3	255 74	30	1.7058	0.1918	66.981°	5.248°
20LH23_4	014 30	30	1.4874	0.1302	156.161°	9.412°

*Orientation given as strike and dip.

N = Number of Ellipses Selected

▨ = 95% Confidence Intervals

Three-Dimensional Best-Fit Ellipsoids

		Robin		Shan	
Max. (A)	**Length (Å)**	1.324	0.062	1.327	0.065
	Trend	264.33°	28.62°	262.22°	30.15°
	Plunge	62.42°	4.92°	62.35°	5.08°
	α		14.44°		15.34°
Int. (B)	**Length (Å)**	1.043	0.052	1.044	0.053
	Trend	168.98°	10.96°	168.69	11.32°
	Plunge	2.79°	11.91°	1.84	12.93°
	α		15.46°		16.11°
Min. (C)	**Length (Å)**	0.724	0.029	0.722	0.029
	Trend	77.53°	10.84°	77.73°	11.05°
	Plunge	27.41°	3.62°	27.58°	3.58°
	α		9.96°		10.13°

α = Angular Error

▨ = 95% Confidence Intervals

20LH24C

Two-Dimensional Best-Fit Ellipses

	Orientation*	N	R		φ	
20LH24C_1	196 82	60	1.1281	0.1045	95.683°	23.732°
20LH24C_2	094 52	60	1.6542	0.1227	81.440°	4.980°
20LH24C_3	293 41	60	1.6315	0.1356	76.200°	4.702°

*Orientation given as strike and dip.

N = Number of Ellipses Selected

▨ = 95% Confidence Intervals

Three-Dimensional Best-Fit Ellipsoids

		Robin		Shan	
Max. (A)	**Length (Å)**	1.247	0.069	1.244	0.073
	Trend	142.13°	80.89°	129.71°	84.06°
	Plunge	80.80°	34.02°	82.85°	34.72°
	α		37.59°		35.58°
Int. (B)	**Length (Å)**	1.128	0.055	1.131	0.058
	Trend	359.51°	5.87°	359.35	5.88°
	Plunge	7.34°	35.30°	4.65	36.73°
	α		37.64°		38.63°
Min. (C)	**Length (Å)**	0.711	0.026	0.711	0.026
	Trend	268.80°	4.82°	268.90°	4.83°
	Plunge	5.53°	3.99°	5.43°	3.96°
	α		5.52°		5.52°

α = Angular Error

▨ = 95% Confidence Intervals

APPENDIX C: COMPREHENSIVE FAULT DATA

	Station	**Fault Planes**		**Slickenlines**		**Slip Sense**	**Pop***
		Strike	Dip	Trend	Plunge		
Mount Watson Fault Zone	20MW40	341	21	-	-	-	2
		225	04	-	-	R	3
		038	52	355	02	-	-
		319	18	046	12	-	2
		356	30	-	-	-	2
		351	28	140	26	-	2
		185	20	178	02	R	1
		075	25	187	24	-	2
		270	07	211	05	-	3
		260	06	081	21	-	3
		122	86	105	21	-	-
		265	39	040	22	-	-
		252	08	330	08	-	3
		358	13	021	06	-	2
		218	16	332	16	-	3
		165	12	330	03	-	1
		104	56	-	-	-	-
		014	21	-	-	-	2
		025	17	-	-	-	2
		030	20	-	-	-	2
		355	22	-	-	-	2
	20MW41	180	14	190	04	R	1
	20MW43	58	76	69	37	-	-
		110	20	224	20	R	3
		155	76	-	-	-	-
		45	63	-	-	-	-
	20MW44	170	26	215	20	R/S	1
		136	12	250	6	R/S	1
		136	12	230	2	-	1
		208	4	-	-	-	3
		310	18	-	-	-	2

	Station	Fault Planes		Slickenlines		Slip Sense	Pop*
		Strike	Dip	Trend	Plunge		
Borland Road Fault Zone	20BR55	175	19	183	3	-	-
		098	87	275	44	-	3
		086	89	265	43	-	3
		087	72	258	25	-	3
		154	45	263	34	-	2
		101	40	221	40	-	1
		108	29	-	-	-	1
		139	22	199	19	-	1
		109	35	200	24	-	1
	20BR57	325	89	-	-	-	2
		320	84	326	44	-	2
		170	25	326	12	-	1
		017	76	-	-	-	3
		015	78	-	-	-	3
		007	85	-	-	-	3
		121	85	-	-	-	-
		119	87	-	-	-	-
		157	88	-	-	-	-
		166	61	-	-	-	-
		209	22	-	-	-	1
		198	25	-	-	-	1
		192	31	-	-	-	1
		336	87	-	-	-	2
		332	88	-	-	-	2
		331	86	-	-	-	2
	20BR58	107	74	-	-	-	2
		129	69	152	40	-	2
		110	80	-	-	-	2
		118	70	295	9	D	2
		073	42	-	-	-	3
		078	43	-	-	-	3
		084	23	-	-	-	3
		091	37	-	-	S	3
		170	32	320	15	-	1
		196	29	317	27	-	1
		199	36	296	36	-	1
		093	44	-	-	-	3

	Station	**Fault Planes**		**Slickenlines**		**Slip Sense**	**Pop***
		Strike	Dip	Trend	Plunge		
Borland Road Fault Zone (Cont.)	20BR58 (cont.)	221	53	-	-	-	-
		227	41	-	-	-	-
		165	43	255	37	-	1
		181	30	-	-	-	1
		278	71	-	-	-	-
		186	65	-	-	-	-
		191	64	-	-	-	-
		275	81	-	-	-	-
		192	54	-	-	-	-
		282	75	-	-	-	-
		152	32	-	-	-	1
		242	77	-	-	-	-
		185	54	-	-	-	-
		279	64	-	-	-	-
		193	78	-	-	-	-
		143	45	-	-	-	1
		096	28	-	-	-	3
		131	33	-	-	-	1
		140	34	-	-	-	1
		096	31	-	-	-	3
		091	29	-	-	-	3
		240	73	-	-	-	-
		165	49	329	17	-	1
		187	70	-	-	-	-
		137	80	-	-	-	2
		141	74	-	-	-	2
		098	22	-	-	-	3
		092	44	-	-	-	3
		097	42	-	-	-	3
		103	36	-	-	-	3
		084	23	-	-	-	3

	Station	**Fault Planes**		**Slickenlines**		**Slip Sense**	**Pop***
		Strike	Dip	Trend	Plunge		
Monowai Fault Zone	20LM32	153	71	-	-	-	1
		144	73	330	8	-	1
		019	58	164	43	-	-
		230	46	240	16	-	-
		308	55	110	15	-	3
		004	60	174	17	-	-
		158	65	162	9	-	1
		220	80	225	28	-	-
		299	51	267	42	-	3
		307	82	122	32	-	-
		265	84	82	25	-	-
		306	86	123	33	-	-
		160	58	157	2	-	1
		152	59	-	-	-	1
		321	78	122	11	-	-
		318	82	124	11	-	-
		313	59	121	27	-	3
		315	58	125	26	-	3
		205	20	-	-	-	-
		194	77	201	23	-	-
		314	61	-	-	-	3
		021	59	064	49	-	-
		032	62	065	46	-	-
		316	45	-	-	-	3
	20LM33	230	80	243	53	-	-
		222	80	236	55	N/S	-
		250	89	236	55	-	-
		244	88	241	54	-	-
		243	88	245	52	-	-
		231	82	244	58	-	-
		232	83	-	-	-	-
		229	87	225	53	-	-

	Station	Fault Planes		Slickenlines		Slip Sense	Pop*
		Strike	Dip	Trend	Plunge		
Monowai Fault Zone (Cont.)	20LM34	148	72	238	72	R	-
		224	55	043	2	-	-
		210	85	214	40	D	2
		140	52	142	2	-	-
		009	44	174	14	S	-
		181	60	227	52	-	-
		206	84	213	50	-	2
		217	85	221	40	-	2
		063	60	134	59	-	1
		200	86	202	25	-	2
		160	52	201	40	-	-
		140	52	142	2	D	3
		140	56	142	3	D	3
		142	53	144	3	D	3
		181	60	-	-	-	-
		191	51	179	15	S	-
		058	58	-	-	-	1
		181	41	-	-	-	-
	20LM36	247	66	-	-	-	-
		228	81	-	-	-	-
	20LM37	117	84	297	5	-	-
Eel Creek Fault Zone	20LH49	010	48	254	40	-	-
	20LH50	170	66	340	21	D	1
		164	60	330	24	D	1
		185	84	-	-	-	1
		170	72	346	29	-	1
		176	64	345	22	-	1
		295	80	315	63	-	2
		169	62	143	64	-	1
		178	65	146	63	-	1
	20LH51	264	74	301	65	-	2
	20LH52	313	78	127	25	-	2
		284	52	308	21	-	2

	Station	Fault Planes		Slickenlines		Slip Sense	Pop*
		Strike	Dip	Trend	Plunge		
Hauroko Fault Zone	20LH01	216	55	320	52	-	-
		269	18	128	22	R	3
		062	61	132	34	-	-
	20LH02	342	72	162	12	-	-
		234	61	075	54	-	-
	20LH20	092	81	266	32	S	2
		096	72	210	70	R	2
		255	80	204	77		3
		285	67	285	67	D	3
		285	68	-	-	-	3
		095	81	-	-	-	2
	20LH21	105	80	276	40	R	2
		110	75	-	-	R	2
		090	71	090	0	R	2
		114	65	173	60	S	2
		105	78	135	67	S/R	2
		100	80	277	16	-	2
		065	75	-	-	R	1
		055	70	-	-	R	1
		245	54	-	-	-	3
		235	74	-	-	-	3
		227	74	-	-	-	3
		174	53	-	-	-	-
		209	48	-	-	-	-
		252	78	-	-	-	3
	20LH22	354	74	130	64	S9	-
		064	69	212	54	D	-
		135	58	343	35	R/D	-
	20LH23	297	75	-	-	-	-
	20LH24	144	62	157	7	S	-
		220	80	-	-	-	-

	Station	Fault Planes		Slickenlines		Slip Sense	Pop*
		Strike	Dip	Trend	Plunge		
Hauroko Fault Zone (Cont.)	20LM32	088	60	94	22	-	1
		071	52	161	4	-	1
		090	51	153	6	-	1
		078	53	161	8	-	1
		085	60	096	18	-	1
		082	58	094	21	-	1
	20LM34	062	64	164	64	R	1
		084	64	196	62	R	1
		065	57	212	40	S	1
		063	55	166	55	-	1
		060	55	174	53	-	1
		057	84	220	71	-	-

R = Reverse
N = Normal

D = Dextral
S = Sinistral

* The three largest fault populations discerned for each fault zone are designated from 1 (population used for fault kinematic analysis) to 3.